Study of Solid State Photocatalysts and other Energy Materials using Synchrotron Radiation

A Thesis Submitted to the

College of Graduate Studies and Research

in Partial Fulfillment of the Requirements

for the degree of Master of Science

in the Department of Physics and Engineering Physics

University of Saskatchewan

Saskatoon

By

Eamon J. G. McDermott

Permission to Use

In presenting this thesis in partial fulfilment of the requirements for a Postgraduate degree from the University of Saskatchewan, I agree that the Libraries of this University may make it freely available for inspection. I further agree that permission for copying of this thesis in any manner, in whole or in part, for scholarly purposes may be granted by the professor or professors who supervised my thesis work or, in their absence, by the Head of the Department or the Dean of the College in which my thesis work was done. It is understood that any copying or publication or use of this thesis or parts thereof for financial gain shall not be allowed without my written permission. It is also understood that due recognition shall be given to me and to the University of Saskatchewan in any scholarly use which may be made of any material in my thesis.

Requests for permission to copy or to make other use of material in this thesis in whole or part should be addressed to:

Head of the Department of Physics and Engineering Physics
116 Science Place
University of Saskatchewan
Saskatoon, Saskatchewan
Canada
S7N 5E2

Abstract

This work presents a spectroscopic and theoretical study of several energy materials using synchrotron-based techniques. Two classes of materials are studied: solids that have reported photocatalytic properties, and lithium compounds that are thought to form during the cycling of modern battery electrodes.

An overview of synchrotron soft X-ray spectroscopic techniques is presented, along with the theory and procedures associated with performing such measurements. These measurements are compared to density functional theory (DFT) calculations, as implemented by the WIEN2k package, along with a description of the DFT method. Calculated electronic structure is shown to be a useful aid in interpreting the results of X-ray emission and X-ray near-edge absorption measurements (XES and XANES), allowing conclusions about the physical structure and properties of the materials to be reached.

Two photocatalytic systems are outlined, the first of which is a solid solution of GaN and ZnO (GaN:ZnO) that exhibits an unexpected reduction in band gap. By carefully comparing common hybridized features from O, N and Zn core emission lines, a binding energy picture of the valence and conduction bands of GaN:ZnO is constructed, allowing its band gap reduction to be described as a consequence of heterojunctions between predominantly GaN and ZnO regions within the solid solution. This description attempts to resolve controversy in the literature regarding the origin of the band gap reduction, as well as to rule out a hypothesized oxynitride superlattice structure as the explanation.

The second photocatalytic system studied is a carbon nitride derivative, poly(triazine imide) (PTI) that displays high crystallinity and that could be very inexpensive to produce due to its elemental abundance. Through resonant excitation, two inequivalent N sites in PTI can be probed by X-ray emission spectroscopy, indicating the material is not a conjugated polymer like other reported carbon nitrides. The band gap of the system is observed to decrease in response to disordered Li loading, an effect that is confirmed by DFT calculation. Several potential disorder models of the Li loading of PTI are investigated with DFT force minimization in order to choose a structural candidate capable of producing calculated X-ray spectra that agree with our measurements.

The presented lithium study attempts to use a modern soft X-ray absorption facility to characterize the Li surface by-products inherent to the charge-discharge cycling of a battery electrode. A survey of potential Li compounds was performed using Li K-edge XANES will be compared to DFT calculations and X-ray Raman Scattering measurements performed by collaborators in the future. Correlating measurements of the survey compounds with charge-cycled electrode measurements will be an area for future work.

Acknowledgements

I gratefully acknowledge my supervisor, Dr. Alexander Moewes for the incredible support he has provided me in the course of my studies under him.

I would like to acknowledge the members of my research group for their collaboration and for sharing their experience and expertise during late night measurement sessions, heated discussions at group meetings and at lunches. I acknowledge Robert Green and Teak Boyko for their measurements of GaN:ZnO materials and John McLeod for his assistance in measuring lithium samples.

I greatly appreciate the contribution to this work by my collaborators who synthesized samples for measurement, organized research projects and provided their input on my work. To this end I acknowledge Dr. Ernst Z. Kurmaev, Prof. Kazuhiko Maeda, Prof. Kazunari Domen and Larissa Davydovna Finkelstein for their contributions to my work on GaN:ZnO, Prof. Dr. Wolfgang Schnick, Eva Wirnheir and Prof. Jens Müller for their contributions to my work on PTI and Dr. Jordi Cabana and Dr. Ulrike Boesenberg for their contribution to my work on lithium compounds.

This work was supported by funding from the National Science and Engineering Research Council (NSERC) of Canada, the Canada Research Chair program and the Graduate Teaching Fellowship program of the University of Saskatchewan. Research was performed at the Advanced Light Source, located at the Lawrence Berkeley National Laboratory, Berkeley, California, USA. The Advanced Light Source is supported by the Director, Office of Science, Oiffice of Basic Energy Sciences, of the U.S. Department of Energy under Contract No. DE-AC02-05CH11231. My research was also conducted at the Canadian Light Source located in Saskatoon, Saskatchewan, Canada. The Canadian Light Source is supported by NSERC, the National Research Council Canada, the Canadian Institutes of Health Research, the Province of Saskatchewan, Western Economic Diversification Canada, and the University of Saskatchewan.

I acknowledge Tom Reigeir, Lucia Zuin, Ning Chen, Wanli Yang, Darren Hunter and all other beamline personnel for invaluable assistance during the course of my experimental work at the Advanced Light Source and the Canadian Light Source facilities.

Contents

List of Tables

List of Figures

List of Abbreviations

ALS	Advanced Light Source
CLS	Canadian Light Source
DFT	Density Functional Theory
DOS	Density of States
LBNL	Lawrence Berkeley National Laboratory
Linac	Linear Accelerator
NMR	Nuclear Magnetic Resonance spectroscopy
PDOS	Partial or Projected Density of States
PTI	poly(triazine imide) material
RXES	Resonant X-ray Emission Spectroscopy
SHE	Standard Hydrogen Electrode
TEY	Total Electron Yield
TFY	Total Fluorescence Yield
UHF	Ultra High Frequency (300 MHz - 3 GHz)
UV-Vis	Ultraviolet-Visible reflectance spectroscopy
VLS PGM	Variable Line Spacing Planar Grating Monochromator
XANES	X-ray Absorption Near Edge Structure
XAS	X-ray Absorption Spectroscopy/Spectrum
XES	X-ray Emission Spectroscopy/Spectrum
XRD	X-ray Diffraction crystallography
XRS	X-ray Raman Scattering

Chapter 1

Introduction

Photocatalytic materials are an emerging class of substances that facilitate redox reactions in the presence of solar illumination without being consumed in the process . Unlike traditional catalysts, which provide a pathway for chemicals to react at a faster rate than is possible without the catalyst present, photocatalysts are able to absorb energy from incident photons in order to drive reactions that do not spontaneously occur. By driving reactions using light, photocatalysts have the potential to facilitate some electrochemical reactions that are currently uneconomical, such as the hydrolysis of water [1, 2] or the breakdown of environmentally hazardous organics [3–5]. If appropriate photocatalysts could be developed that operate at high quantum efficiency under solar illumination, a cheap source of hydrogen gas for energy storage purposes could be realized. This application provides ample motivation for the careful study of this class of materials using the best research tools available, including soft X-ray spectroscopy at bright synchrotron facilities.

This exciting discovery of an organic photocatalyst by Wang *et al.*[6], along with the low band gap and high reported H_2 yield of a solid solution of GaN:ZnO by Maeda *et al.*[7], combined with world events revolving around peak oil production, have contributed to a revival of research into photocatalysis, a field that had seen little activity since the 70's and 80's. Since Wang's publication, reports have described advancements in other photocatalytic systems, such as titania[8], In_2O_3 [9], various organic complexes with Ru, Rh and Pd [10, 11] and various composite organic molecules [12–14].

If an appropriate, economic photocatalytic material could be produced, it may become possible to build large-scale solar powered water splitting reaction facilities. In the reactor, a supply of water would be fed over a photocatalyst suspended in a solar collector array, releasing H_2 and O_2 gas to be collected and stored for subsequent use. This process would

complement the capture of solar energy by photovoltaic cells as unlike electricity, hydrogen could be stored as it is produced and used on demand, a prospect which is not readily feasible with electrical energy. The co-production of hydrogen and electricity from solar energy is seen by some as the most obvious step in transitioning away from a carbon-fuel economy to a hydrogen economy [15].

This work investigates the electronic properties of photocatalytic materials using synchrotron-lit soft X-ray spectroscopy. Using X-ray Absorption Near Edge Spectroscopy (XANES) and X-ray Emission Spectroscopy (XES) it is possible to directly probe the near-Fermi level electronic structure of solid materials in an element and site specific manner. The measured spectra provide an approximation of the Density of States (DOS) available to be occupied by electrons in a material, information that provides details of the physical behaviour of the material. By studying electronic structure in this way it is possible to determine the band gap of very small quantities of material with comparable accuracy to other techniques. The ability to acquire detailed information from small quantities of sample material makes soft X-ray spectroscopy a valuable tool in the investigation of novel materials or material phases that are difficult to synthesize or must be studied in low concentrations.

The present work details the results of a study of the GaN:ZnO solid solution, a candidate photocatalyst with . This work, recently published in the Journal of Physical Chemistry C [16], consisted of an X-ray spectroscopic study of GaN:ZnO at various concentrations, a theoretical model using density functional theory, and a novel analysis of this material as a heterojunction solid solution. Also presented is a study of poly(triazine imide), a candidate photocatalyst similar in structure to a material reported by Maeda *et al.* but with indications of a lower band gap. Significant theoretical modelling has been undertaken to present an electronic structure of this material that agreed with experimental measurements.

Hydrogen production by photocatalysis is only one possibility for storing solar energy available to be studied using soft X-ray spectroscopy. Currently a considerable amount of solar photovoltaic capacity exists internationally that is being used to power national electrical grids. However, the capacity of solar photovoltaics to power our economy is limited due to its intermittent generating capacity, and there currently exist very few methods to store grid-level electricity at any appreciable scale. However, battery technologies are currently receiving

considerable research attention, and recent breakthroughs in lithium alloying electrodes [17], particularly silicon electrodes [18] have raised the potential of increasing battery capacity by the orders of magnitude necessary to make them viable for grid-level storage. However, understanding the nature of lithium reactions in these materials is hampered by a poor understanding of its chemical properties and a limited set of experimental methods with which to study its chemical speciation. However, as our research group has ready access to an instrument capable of characterizing Li species by X-ray absorption spectroscopy, the VLS PGM beamline at the Canadian Light Source, a collaboration was formed with researchers at LBNL to study the side-products of electrochemical cycling of Li onto battery electrodes. This attempted study led to a survey of various lithium compounds which we are working to characterize by both XANES and X-ray Raman Scattering, the experimental results of which are presented in this work.

This thesis is presented in 7 main chapters. In Chapter 2 the basic theory of condensed matter physics necessary to discuss the remaining material and calculations is outlined. Chapter 3 introduces concepts of synchrotron radiation, while chapter 4 discusses the experimental techniques these facilities allow. Chapter 5 gives an introduction to the relevant electrochemical theory necessary in the study of photocatalytic materials. Chapter 6 discusses the GaN:ZnO solid solution photocatalyst including experimental results, theoretical calculations and analysis. Chapter 7 similarly discusses the poly(triazine imide) candidate photocatalyst. Chapter 8 discusses the preliminary results of our survey of lithium compounds] as well as outlining some future directions that study will take.

Chapter 2

Relevant Condensed Matter Theory

The spectroscopic techniques described below depend on a foundation of condensed matter physics and its quantum mechanical theory. Quantum mechanics, through a number of approximations and with varying degrees of accuracy, can be used to describe many observable properties of solids, such as their physical and electronic structure, electrical and thermal conductivity and the effects of photoexcitation.

2.1 Quantum Mechanical Basis of Condensed Matter Physics

The field of condensed matter physics can be considered the study of concentrated groups of atoms and the interaction of their electrons with the nuclear potentials in the region. Electrons can be described quantum mechanically as negatively charged waves [19]. These waves can either be free to translate through space as a wave packet or bound to a potential well as a stationary wave. Electron dynamics can be described non-relativistically by the Schrödinger equation [20]:

$$\mathbb{H}\psi = E\psi \tag{2.1}$$

Solutions ψ to the Schrödinger equation satisfy the physical interactions described by the Hamitonian $\mathbb{H}$, and have characteristic eigenenergies E. The ψ themselves describe the complex probability distribution of the electron within a particular co-ordinate or observable basis. The Schrödinger equation can therefore be used to describe the energy states of quantum mechanical systems, and for time-dependant Hamiltonians, their evolution with time.

Several important properties of matter emerge from the form of solutions to Schrödinger's

equation, including the discrete energy states that emerge when electrons are bound to a nucleus. When bound, electrons preferentially occupy the lowest energy states available, separating into stationary waves with discrete characteristic energies [19]. This result is the chief departure quantum mechanics makes from classical mechanics, which assumed a universe in which matter could take on continuous energy or momentum regardless of the local environment.

In a condensed matter system, $\mathbb{H}$ will consist of kinetic propagation terms for each electron and nucleon, nuclear potential terms, electron-electron interactions (such as spin pairing and exchange), and other terms as may be necessary to describe the dynamics of the system. A Hamiltonian without spin pairing can be written as

$$\begin{aligned}
\mathbb{H} &= -\mathbb{T}_{electron} - \mathbb{T}_{nucleus} - E_{electron-nucleus} + E_{electron-electron} + E_{nucleus-nucleus} \\
&= -\frac{\hbar^2}{2}\left(\sum_i \frac{\nabla^2_{\vec{r_i}}}{m_e} + \sum_j \frac{\nabla^2_{\vec{R_j}}}{M_j}\right) - \frac{1}{4\pi\epsilon_0}\sum_{i,j}\frac{e^2 Z_j}{|\vec{r_i} - \vec{R_j}|} + \frac{1}{8\pi\epsilon_0}\sum_{i\neq j}\frac{e^2}{|\vec{r_i} - \vec{r_j}|} \\
&\quad + \frac{1}{8\pi\epsilon_0}\sum_{i\neq j}\frac{e^2 Z_i Z_j}{|\vec{R_i} - \vec{R_j}|}
\end{aligned} \tag{2.2}$$

where $\mathbb{T}$ represents the kinetic energy operator, E's are Coulomb interactions, m_e is the electron mass, M_j is the mass of nucleus at $\vec{R_j}$ with elementary charge Z_j, e is the elementary charge and ϵ_0 is the electric constant [21].

Unfortunately, while one can describe a Hamiltonian to arbitrary physical precision, only the Hamiltonians of very simple systems can be solved exactly (as a result of the many-body problem), and it quickly becomes computationally unwieldy to use numeric methods to solve more complex systems. This necessitates the use of approximations to allow more complex systems to be tractable.

2.2 Born-Oppenheimer Approximation

A greatly simplifying approximation that can be immediately made to a condensed matter system is to consider each nucleus to be a positively charged particle that does not deviate from its equilibrium position under the influence of the electrons. It is physically reasonable to make this approximation given the relative masses of electrons and the nuclei they orbit;

even in the lightest element, hydrogen, the nucleus is three orders of magnitude more massive than an electron. Additionally, the spatial extent of the electron states are considerably larger than the charge radius of the nucleus, making the particle approximation reasonable. For example, the hydrogen atomic radius is approximately 0.53 fm while the generally accepted charge radius of a single proton is 0.8768(69) fm [22]

This approximation was first proposed by Max Born and J. Robert Oppenheimer in 1927 to allow the wave functions of molecules to be calculated manually [23]. By considering the Hamiltonian of the system as composed of separable electron and nuclear terms, the wave functions that solve the Schrödinger equation are divided into two independent sets. Assuming the nuclear wave functions are constant over time (i.e. not contributing to the dynamics of the system) then removes the requirement to compute these solutions to describe the electron behaviour. The nuclear contribution to the system can instead be considered as a time-averaged background potential field in which electron interactions occur [21].

The Born-Oppenheimer approximation greatly simplifies the task of describing a condensed matter system, however the solutions to the Schrödinger equation simplified in this manner still involves complex multi-electron functions that are not readily computable.

2.3 Density Functional Theorem

To attempt to solve the many-body electron for a solid, Hohenberg and Kohn took the approach of modelling a self-interacting electron gas under external potential V(r) [24]. Under such an approach, the Hamiltonian can be simplified to only three elements: individual electron kinetic and potential energies and interaction with the external potential. These interactions are described by the equation:

$$\mathbb{H} = \mathbb{T} + \mathbb{U} + \sum_i V(\vec{r_i}) \tag{2.3}$$

It is then possible to rewrite the energy solutions to the Schrödinger equation in terms of the ground state particle density [21]:

$$\begin{aligned} E[n] &= <\psi_o|\mathbb{T}+\mathbb{U}|\psi_o> + \int d\vec{r} n(\vec{r}) V_{ext}(\vec{r}) \\ &= F(n) + \int d\vec{r} n(\vec{r}) V_{ext}(\vec{r}) \end{aligned} \tag{2.4}$$

The benefit of solving the equation in this manner is that the functional, $F(n)$, now contains all the interactions necessary to describe the total energy of the electron gas system independently of the external potential. Furthermore, Hohenberg and Kohn were able to prove both that the ground state density *uniquely* defines the overall potential of a system, and that the *minimum* total system energy is described by the ground state density. Because this ground state density is unique, it is therefore possible (in principle) to relate it to all other physical properties of the system, including the previously unsolvable ground state multi-electron wave function.

Because there is a metric to determine if a density configuration is the ground state density (a minimum total energy), it is possible to procedurally work towards the true ground state density by successively proposing a new density configuration, calculating its total energy, testing whether the total energy has decreased and then continuing with another cycle. Once the change in total energy per cycle becomes arbitrarily small the calculation can be said to have converged on the correct ground state density.

DFT has become a powerful investigative tool in the field of condensed matter physics, but it is not without its shortcomings. The terms of the functional used in calculations will determine the degree to which the solved ground state density corresponds to the true physical density. The only exact functionals for electron correlation and exchange energies are for the free electron gas used as the basis for solving the DFT problem, therefore approximations must be made. The two main classes of functionals used in DFT calculations are those that use the local-density approximation (LDA) and those that use the generalized gradient approximation (GGA). LDA posits that exchange-correlation energy at a point in space depends only on the local ground state particle density; this is true in the case of the free electron gas under constant potential, but not true in a condensed matter system where the potential will vary with the position relative to nuclear charges. GGA attempts to resolve this issue by also taking into consideration the local state density gradient, and generally gives more accurate results than LDA [21].

Other types of hybrid functionals exist, such as those that include exchange terms drawn from other methods for solving the ground state multi-electron wave function problem (for example, the Hartree-Fock method). Additionally, a modified Becke-Johnson potential has

been recently introduced to the WIEN2k DFT code as a more accurate method of calculating material band gaps [25], which GGA has systematic issues with calculating [21].

2.4 WIEN2k Code

Calculations for this work have been carried out with the version 11 release of the WIEN2k code [26]. This code implements a full-potential (linearized) augmented plane-wave (LAPW) method of solving the DFT problem, one of the most accurate methods for representing nuclear potentials within a condensed matter system.

WIEN2k is a user-friendly DFT code package that implements a full calculation work-flow. Crystal structure and symmetry may be described by hand or imported from crystallographic data. After the DFT self consistent calculation cycle has been completed, a number of additional packages can be used to derive physical properties from the calculated ground state particle density, including total density of states, projected density of states for the various atomic sites in the material, simulated X-ray absorption and emission spectra, optical and phonon properties and bandstructure diagrams.

WIEN2k uses an augmented plane wave basis set to represent the electrons of a periodic, crystalline system [21]. This basis set consists of the spherical harmonics in the regions near nuclear charges and Block plane waves in the interstitial regions between nuclei. The two regions intersect at a "muffin-tin" radius at which continuity is enforced. This radius is chosen at the start of the calculation to restrict localized core electrons to the nucleus with which they "belong" while allowing semi-core and valence electrons to delocalize and be described by the plane waves. In order to reduce the number of basis functions necessary to produce a converged set, WIEN2k augments the basis set with "local orbitals": constructed radial functions that are constrained by an appropriate choice of coefficients to zero magnitude and radial derivative at the muffin-tin radius of a particular nucleus. After diagonalizing the system of plane waves, ensuring continuity at the muffin-tin radius, the resulting LAPW basis set can then be used to calculate the state density required to iteratively solve the DFT problem.

WIEN2k evaluates the basis set only at discrete positions in reciprocal crystal space

(k-space). Therefore it is necessary to specify a grid of k-points before beginning a calculation. Since each k-point is evaluated discretely it is possible to parallelize the calculations over a number of processors, one for each k-point, allowing WIEN2k to quickly calculate over large k-point grids provided sufficient resources.

Once a calculation is complete and a sufficiently converged ground state density is found, a comparison between simulated X-ray emission absorption spectra can be compared to actual experimental measurements to determine the validity of the calculated result. By comparing these results, it is possible to judge the validity of the proposed crystal structure used for the DFT calculation. If there is sufficient agreement the DFT calculation can be used as an aid in interpreting experimental results, such as the identification of secondary peaks from hybridizing atoms in an X-ray emission spectrum.

Chapter 3

Synchrotrons and Synchrotron Radiation

Synchrotron light sources provide a powerful experimental probe into the realm of condensed matter physics: the brilliant, coherent monochromatic X-ray beam. Synchrotron radiation was first discovered as somewhat of an accident. It was known that parasitic radiative losses occurred as electron beams were steered around storage rings by bending magnets, but it was not until this light was directed out a window and observed that the true potential of the phenomenon was appreciated.

Two synchrotron sources were used to perform the experiments discussed below: the Canadian Light Source (CLS) located at the University of Saskatchewan, and the Advanced Light Source (ALS) at the Lawrence Berkeley National Laboratory. A brief overview of the physics necessary to describe these facilities is provided below.

3.1 Synchrotron Radiation

The brilliance of synchrotron radiation makes it particularly suitable for research use as it allows for flexibility in the design of experiments. As electrons (or other charged particles) are accelerated around a storage ring at relativistic speeds, the energy necessary to steer them in a curved path is applied by bending magnets. In order for net energy balance to be maintained in the storage ring there must be losses, the largest of which is the radiation of synchrotron light. Synchrotron light is emitted as broad spectrum light emitted in a narrow cone. The frequency emitted by electrons deflected by a magnetic field B can be characterized by the following relationship:

$$\omega = \gamma^2 \frac{eB}{m_e} \tag{3.1}$$

where γ is the Lorentz factor for particle velocity v:

$$\gamma = \frac{1}{\sqrt{1 - \frac{\nu^2}{c^2}}} = \frac{1}{\sqrt{1 - \beta}} \tag{3.2}$$

The angular distribution of the emitted radiation is inversely proportional to γ, causing highly accelerated beams to emit in narrow beams. Because the radiated power is emitted over a small radial cross-section, synchrotron radiation is one of the most brilliant sources of X-ray wavelengths known (although Free Electron Lasers and other fourth generation light sources of greater intensity are under active development). This brilliance allows experimental beamlines to be constructed that can discard undesired photons to produce highly monochromatic beams or extremely small beam spot sizes, giving flexibility not available with tradition X-ray sources.

3.2 Synchrotron Facilities

The two synchrotron facilities used in this study so far, ALS and CLS, are both compact, third generation facilities designed from the ground up to produce light for experimental use. Both designs feature the same basic components, which will be outlined below.

3.3 Linear Accelerator

A linear accelerator (or linac) is used to provide the initial electron beam at both synchrotron facilities in question. In a typical accelerator, an electron gun cathode is oscillated at high voltage and frequency. This stimulation imparts enough energy to the cathode that bunches of electrons will be ejected from its surface, to be directed down a linear vacuum tube. These electron bunches are then accelerated by RF cavities located along the length of the accelerator [27].

A linacs RF cavities also control the bunch shape and duration in addition to accelerating the beam. The CLS linac produces 250 MeV bunchs of between 2 ns and 132 ns in duration [28], while at the ALS, the linac produces 50 MeV bunches between 20 ps and 2.5 ns [29]. The nature of the electron bunches produced at the linac effects the nature of the downstream

radiation produced by the synchrotron. As each electron bunch travels past beamlines they will receive light for the duration of the bunch. This enables synchrotrons to operate in a pulsed mode by only injecting single bunches of electron from the linac. Single-bunch mode can be useful for certain types of experiments where the pulse time can be used as a characteristic evolution time.

By the time it leaves the linear accelerator, an electron beam has already been accelerated to very close to the speed of light, 99.9998% of c in the case of CLS. This beam is then fed to the booster ring for further acceleration.

3.4 Booster Ring

The booster ring accepts the linear accelerator's output beam and accelerates it to the operating energy of the facility: 1.9 GeV at the ALS and 2.9 GeV at the CLS. Acceleration energy in the ring is provided by an RF cavity: a commercial 80kW induction output tube UHF transmitter at ALS [30] and a Cornell design cylindrical superconducting RF cavity at CLS [31] provides the necessary energy input. The RF cavity operates by producing radiowave pulses that are synchronized to electron bunches passing through it, boosting them in energy. It is this synchronization from which the term synchrotron is derived.

Bending magnets are used to steer the accelerated electron beam around the circular path of the booster ring, allowing each bunch of the beam to be accelerated multiple times by the RF cavity. At the ALS a total of 20 sextupole, 32 quadrupole and 24 dipole magnets [32] are used to orbit a nearly circular ring with a circumference of 75 m [33]. The CLS uses 28 quadrupole and 20 dipole magnets to orbit an ovular booster ring with a circumference of 103 m [34].

Once boosted to the facility's operational energy, the electrons in the booster ring are periodically injected into a storage ring for use. The ALS regularly operates in a top-up mode where injection occurs every 30 - 35 seconds to maintain a steady storage ring current [30]. The CLS aims to implement top-up mode in the future, but currently operates on a 12 hour injection schedule; during periods of injection, light is unavailable for experiments.

3.5 Storage Ring

A synchrotron facility's storage ring contains the stable electron beam that is used to produce light for experiments. Like the booster ring, a series of magnets are used to steer electrons around the ring. However straight sections in the ring are also present, containing equipment to generate additional light for experimental beamlines beyond simple bending magnets. By using a storage ring to separate the electron beam used for experiments from the beam undergoing acceleration, beam current can be held stable for experiments that require constant or smoothly changing flux.

The CLS storage ring is 171 m in circumference, consisting of 12 straight sections joined by sets of bending magnets to steer and refocus the beam. The ALS storage ring is slightly larger at 197 m in circumference, again with 12 straight sections. Both facilities use one straight section for an RF cavity and one for the feed-in from the linear accelerator, leaving 10 sections for beamline insertion devices.

3.6 Bending Magnet Radiation

Bending magnets are the simplest source of useful radiation within the storage ring of a synchrotron facility. While dipole magnets are primarily used to steer the accelerated electron beam around the geometry of the ring, it is efficient to use some of the lost radiation for experiments.

The angular spread of bending magnet radiation is not particularly narrow in the electron frame of reference. However, in the lab frame this radiation is compressed into a narrow cone characterized by the half angle:

$$\theta \simeq \frac{1}{2\gamma} \tag{3.3}$$

The vertical divergence (divergence perpendicular to the plane of acceleration) can be approximated as $\frac{1}{\gamma}$.

A bending magnet must have a field strength and geometry particular to the ring it is designed to steer electrons around, therefore the radiation from a bending magnet is not tunable by users for experimental purposes.

Bending magnets produce a broad spread of frequencies that may be characterized by a *critical photon energy* E_c [35]:

$$E_c = \frac{3e\hbar B\gamma^2}{2m_e} = 0.665BE_e^2 \tag{3.4}$$

where B is the bend magnet field strength, e and m_e are the electron charge and mass and E_e is the accelerated electron energy (in GeV). The critical energy can be interpreted as the energy at which half the overall power is radiated as photons of energy greater than E_c and half as photons of energy less than E_c. The critical energy can also be used to estimate the maximum photon energy radiated by a bend magnet - at $4E_c$ the flux is reduced by an order of magnitude from that at E_c.

3.7 Insertion Device Radiation

Many experimental techniques benefit from the high photon flux of synchrotron radiation, but often benefit from radiative power restricted to a narrower frequency range than can be produced using a bend magnet. Additionally a large, multi-user synchrotron requires radiation that can be tuned without altering the overall parameters of the storage ring, which impact all users. These requirements have been met by placing beamline-specific insertion devices into the storage ring. Two general types of insertion device exist: undulators and wigglers.

Both undulators and wigglers operate with the same general geometry: an array of N alternating dipole magnets is used to deflect the electron back and forth in the plane of the storage ring. Each deflection causes electrons to accelerate along a curved path, causing radiation to be emitted (similar to a small bending magnet). The geometry of the insertion device can be described using the magnetic deflection parameter K:

$$K = \frac{eB\lambda_i}{2\pi m_e c} \tag{3.5}$$

where B is the magnetic field strength at the centre of the insertion device and λ_i is the periodicity of the magnetic array [35].

Undulators operate at the low magnetic deflection ($K \simeq 1$). In an undulator, the electron beam receives small deflections from its initial path of flight from the magnetic array. As each deflection is small, the angular width over which radiation emitted is small as well; this causes each magnet in the undulator to create a radiation cone nearly aligned with the beam. As these cones overlap, constructive interference will occur near the axis of the electron beam at observed frequencies of order n (λ_n):

$$\lambda_n = \frac{\lambda_i}{2n\gamma^2}(1 + \frac{K^2}{2}\gamma^2\theta^2) \tag{3.6}$$

where θ is a small off-axis observation angle in the plane of the accelerator ring. Using constructive interference allows an undulator to produce semi-monochromatic light - the most power will be radiated at the fundamental wavelength λ_1 while lesser power can be observed along the undulator axis at odd higher-order harmonics (i.e. λ_3, λ_5, etc). Even-order harmonics have a node at the axis ($\theta = 0$) and are therefore not as useful for illuminating experiments.

Wigglers operate at high magnetic deflection ($K \gg 1$). With a large magnetic field deflecting the electron beam each bend becomes more like deflection within a series of bend magnets, due to multiple radiative harmonics overlap in frequency space. Wigglers therefore tend to produce radiation with a much broader distribution in energy than undulators. Additionally, due to the K^2 dependence in Equation 3.6 wigglers are able to produce much higher energy photons than undulators, making wigglers preferable insertion devices at hard X-ray energies.

One of the most useful properties of insertion devices as a source of illumination for experiments is their energy tunability. By adjusting the physical configuration of the insertion device it is possible to adjust its K parameter and hence the frequency profile of the output radiation. In practice this is usually accomplished by adjusting the B in Equation 3.5 by changing the *undulator gap*, or the distance between the upper and lower array of magnets. Higher undulator gaps will yield lower magnetic fields at the beam and vice versa, providing the necessary control to tune the generated light.

The spectroscopic beamlines used in this study, the Spherical Grating Monochromator (SGM) beamline at the Canadian Light Source and Beamline 8.0.1 at the Advanced Light

Source, both use undulator-type insertion devices to produce soft X-rays. SGM uses a 53 pole planar undulator with period $\lambda_i = 45mm$ capable of photon energies between 250 and 2000 eV [36]. Beamline 8.0.1 uses an 89 pole undulator array with period λ_i of 5 cm to achieve an energy range of 70 to 1200 eV [37].

3.8 Monochromators

While undulator-type insertion devices can be used to generate brilliant radiation with a low spectral bandwidth, it is usually necessary for spectroscopic experiments to use downstream optics to further select for the desired wavelength of life. This task is typically achieved in the X-ray region through a *monochromator* - the combination of a user-adjustable *grating* rotated to diffract the desired wavelength when illuminated by incoming light, and *entrance* and *exit slits* that geometrically reject undesirable wavelengths.

Both beamlines used in this study feature spherical gratings as the diffractive component of their monochromator. Diffraction through a grating is governed by the equation

$$m\lambda D = (sin\alpha + sin\beta) \tag{3.7}$$

where m is the order diffracted radiation, λ is the diffracted wavelength, D is the density of ruled lines on the grating and α and β are the incoming and outgoing angles measured with respect to the grating normal [38]. While the relation between α and β is determined by the geometry of the beamline, they are influenced by the rotation of the grating such that a desired wavelength can be selected. With proper calibration, the desired wavelength will be directed down the beamline to be used to light experimental samples.

Wavelengths other than desired will be diffracted at slightly different wavelengths due to defects in the diffraction grating, off-axis radiation from upstream and higher order diffractions. Therefore, to further select for the desired wavelength an exit slit is placed in the beam path at a position that satisfies the *Rowland circle* geometry. In this geometry, the diffractive grating as well as the monochromator entrance and exit slits are placed on the radius of a Rowland circle with radius half that of curvature radius of the grating. This geometry ensures the exiting X-rays remain focused and allows beam bandwidth to be controlled using the width of the exit slit, as closing the slit will trade beam flux for improved monochromaticity.

Chapter 4

Synchrotron Measurement Techniques

In order to investigate the properties of a physical system it is useful to have a measurement tool that operates on the same length or energy scale as that of the system. For investigation of matter at the atomic scale the X-ray is such a tool. X-ray wavelengths are comparable to the atomic radius, making them useful in scattering measurements, and X-ray energies cover the range of the atomic core binding energies, allowing investigation of core level electronic structure of materials. This study uses the later property of soft X-rays (X-rays of energy 50 - 2000 eV) to study the electronic structure and density of states of materials using two techniques: X-ray Absorption Near Edge Structure (XANES) and X-ray Emission Spectroscopy (XES). These techniques will be briefly described below.

4.1 Interaction of X-rays with Matter

An X-ray directed at condensed matter may undergo two interactions of interest to this study: *scattering* and *absorption* [38]. In the case of a scattering interaction, an incoming X-ray can be directly related to an outgoing X-ray that will have a modified momentum (elastic scattering) or a modified momentum and energy (inelastic scattering) [39]. In the case of absorption the incoming X-ray is lost and its energy is transferred to the matter, usually an electron [40]. If the X-ray does not undergo any interaction, but instead continues in a straight path, it can be said to be *transmitted* through the sample.

Any incident X-ray beam that can be directed on to a sample will have both a characteristic spot size and penetration depth (or complete penetration in the case of transmission measurements). The product of these will give an interaction volume in which measurable interactions will occur; this can be considered a characteristic unit of volume with which to

compare measurements of different samples or sample geometries. On the beamlines used in this study there was little user control available to modify the beam spot size; while exit slits could theoretically affect the distribution of light over the beam spot the focal length was not under user control. However, the penetration depth in a solid will depend strongly on the incident X-ray energy, especially as that energy is swept across the absorption edge energies of atoms present in the material. This relation is not simply described, however tools such as the Henke X-ray attenuation length calculator can be used to estimate penetration depths for materials of known composition and density [41].

When performing synchrotron based measurements, X-ray interaction processes occur in very large numbers, and so we must consider experimental results as statistical processes. As a collection of states will be interacted with during an experiment, the resulting measurement will be a function of the density of states (DOS) at a given excitation energy in the system under study. With some understanding of the physical structure of the interaction volume (for example, by assuming its crystal structure) one can extrapolate the DOS structure within limits of certainty and noise. Thus a normalized absorption or emission experiment should be comparable to DOS and X-ray spectra calculated using DFT, a relation that will be exploited in the remainder of this study.

During absorption events within a solid, energy and momentum must be conserved within the system, placing constraints on the allowed transitions. As discussed above, the quantum mechanical nature of matter restricts electrons to occupying discrete energy states while bound to a nucleus. As a result of this, absorption events are only energetically possible when the energy difference between an absorbing electron and the final state to be occupied is the same as the incident X-ray energy. Additionally, interactions between electrons and the electromagnetic field primarily cause dipole transitions in which the total angular momentum must be conserved [42]. As an X-ray photon is a boson with spin ± 1, only transitions with $\Delta l \pm 1$ are allowed in the dipole approximation (for example, $1s \rightarrow 2p$) [40]. Quadrupole transitions may also occur as a result of X-ray absorption events with significantly lower probability [43], but occur primarily within transition metals and are not important to this study at this time.

4.2 X-Ray Absorption Near Edge Spectroscopy (XANES)

By exciting a material with X-rays at energies slightly below the core binding energy of its constituent elements it is possible to excite core electrons into states above the Fermi energy that are normally unoccupied. These unoccupied states are typically referred to as conduction band states in solid state physics, as their partial occupation is the origin of conductivity in metals and semiconductors. Of primary interest in this study are low-energy conduction band states that are still of low enough energy to either be bound to an individual atom (*localized states*) or bound to the solid as a whole (*delocalized states*). Beyond the binding energy, electrons will be excited to states above those that are discretely quantized by the presence of the nuclear potential in the solid; these unbound *continuum states* are of interest in other spectroscopic techniques such as Extended X-Ray Absorption Fine Structure Spectroscopy (EXAFS) and X-ray Photoelectron Spectroscopy (XPS).

Because XANES relies on core level electrons transitioning to conduction band states, the DOS may only be probed by dipole allowed transitions of $\Delta l = \pm 1$. This so called *partial density of states* (pDOS) can be related to DFT calculation as an intermediary for investigating the full density of states. To calculate the pDOS for an atomic site, the wave functions derived from the converged ground-state particle density in that volume must be projected on to atomic-like orbitals with the appropriate symmetry. As a result the pDOS may also be referred to as the *projected density of states* [26].

A necessary effect of exciting a core electron into the conduction band through the absorption process is that a vacancy is left behind at the core level. This vacancy, referred to as a *core hole*, will necessarily distort the ground state configuration of electrons in any material system. Intuitively, the presence of a core hole on an atomic site will decrease the degree to which the nucleus is screened, leading to an "attraction" of electron conduction band states to lower binding energy. XANES is therefore useful only as a probe of the projected DOS of such an excited system by the final state rule, which posits that the shape of a measured spectrum will be determined by the final state of the transition being measured [44].

However, there is still utility in measuring excited states, as they can be related to ground states by interpreting the electronic states found performing DFT calculations.

To perform a XANES measurement, a sample is placed in the path of a suitably monochromatic X-ray beam which is scanned in energy across the absorption edge of the element(s) of interest. At several discrete points in energy, measurements of the absorption coefficient $\mu(E)$ can be collected through a variety of detection techniques. The best measure of $\mu(E)$ is collected by measuring the X-ray beam intensity both before (I_0) and after (I_t) interaction with a sample of thickness t. This type of X-ray transmission measurement yields the linear absorption coefficient through the Beer-Lambert law [45]

$$\mu(E) = \frac{1}{t} ln \left(\frac{I_0(E)}{I_t(E)} \right) \tag{4.1}$$

A transmission measurement is considered the most thorough measurement of the absorption process for most circumstances. However, to perform transmission measurements one requires a uniformly thin sample that can be fully penetrated by a detectable fraction of the X-ray beam. The interaction volume will extend through the entire material, meaning that surface effects will not play a significant role in the measurement of macroscopic samples. However, transmission measurements are very difficult to perform at soft X-ray energies as the sample attenuation is so high (X-rays penetrate only as much as a few micron). It is therefore more practical to measure other processes within the material that relate to the X-ray absorption.

When a core hole is created by X-ray excitation, it has a very short lifetime and will rapidly be refilled by the relaxation of another electron in the vicinity. This leads to a cascade of electrons decaying by various processes one after another until the volume about the original core hole returns to its ground state. In the interior of a sample this decay cascade can proceed entirely within the confines of the system being measured, as the excited electron that previously occupied the core hole will eventually decay to a ground state below the Fermi level while the core hole will be refilled by another electron in the vicinity. However, near the surface of a sample (approximately 2 nm deep at excitations below 1000 eV [46]), there is a probability that an excited electron will be ejected from the sample surface entirely. To maintain charge balance in these circumstances, a sample can be grounded to replenish

electrons that are excited away from the system. The current replacing charge from ground will therefore be related to the number of X-ray absorption events that occur, which is in turn related to the density of conduction band states that electrons will occupy after absorbing electrons. By measuring this current as a function of excitation energy the *total electron yield* (TEY) current I_{TEY} can be found. Measuring a TEY signal requires a relatively conductive sample, but can be a source of good measurements with excellent surface sensitivity due to the low electron escape depth.

All energy released during electron decay cascade processes as described above must be conserved, and some will be re-emitted as X-rays of various energies at or below the excitation energy (the majority of the energy is lost to Auger electrons in the cascade mentioned above). By measuring the intensity of emitted X-rays across some solid angle using a high-voltage channeltron or a spectrometer the *total fluorescence yield* (TFY) can be related to excitation energy in much the same way as TEY measurements. The information in a TFY measurement originates from the full interaction volume of the excitation beam, giving a bulk sensitive measurement. However, this information must be carried from the bulk of the material via X-rays which can themselves be re-absorbed; this effect is known as *self-absorption*. The self-absorption effect is obviously strongest at emission energies that exhibit the strongest primary absorption, leading to spectra where the more intense absorption peaks are suppressed.

4.3 XAS Core-Hole Effect

The presence of a core-hole in the final state of an absorption measurement will in general cause the unoccupied states at the site to be more tightly bound to the nucleus. This results in the measured density of states to be shifted to lower energy. This magnitude of this effect can be estimated by introducing a core hole into a DFT calculation and noting the difference in the ground-state conduction band onset as compared to the onset energy without a core-hole. Our research group has found that calculating a core-hole shift in this way can be used to use XAS to make band gap estimates that are in good agreement with other experimental techniques such as UV/Vis reflectance [47].

4.4 X-Ray Emission Spectroscopy (XES)

When a core-level hole is created through an X-ray absorption process, there is additional information to be gained from the subsequent fluorescent decay. During decay there is a small but significant probability that a valence level electron on the same atom will be the one that fills the hole. This transition will emit a photon with an intensity characteristic of the partial density of states of the valence level at a binding energy equivalent to the photon's energy. Additionally, because of the final state rule, a spectrum of such emitted photons will be characteristic of the ground state density, as opposed to the excited density measured by XANES. By resolving the emitted photons in energy and counting them, an elementally specific spectrum characteristic of a material's valence states can be collected. This technique is known as *X-ray Emission Spectroscopy* (XES).

In order to capture an emission spectrum it is necessary to be able to discriminate between emitted X-rays of different energies with high energy resolution. In the course of this research, this was accomplished through the use of the Rowland-circle geometry spectrometer on Beamline 8.0.1 at the ALS. By allowing emitted X-rays to enter the spectrometer through an entrance slit and diffract off a spherical grating, the X-rays are directed at different angles according to the grating equation (Equation 3.7). The energy range of the beamline is covered by four gratings: two lower energy gratings with radius 5m and 600 and 1500 lines/mm and two higher energy gratings with radius 10m and the same linear density [37]. A glancing angle detector is then used to collect the diffracted X-rays and record the spectrum. This spectrometer achieves a resolving power of $E/\Delta E$ of approximately 1000 [48], equivalent to ≈ 0.4 eV resolution near the nitrogen K line (≈ 400 eV).

XES allows for reasonably direct observation of the occupied ground state of a material, unusual in experimental physics which usually requires the observation of some particle or photon leaving an excited state system. While the resolving power of the spectrometer used to observe emitted X-rays will affect the resolution of the measurement, the degree of precision to which the ground state can be observed is *intractably* limited by the lifetime of the excited core-hole [49]. As time and energy scales are related by the uncertainty principle, the short core-hole lifetime limits the resolution to which we can resolve valence band states

in energy using XES, causing *lifetime broadening* of the measured spectral features. Lifetime broadening is also a factor in XANES measurements, however the lifetime of a bound electron in the conduction band is many orders of magnitude longer than that of a core-hole, greatly decreasing the effect.

Chapter 5

Electrochemical Theory of Photocatalysis

As the main subject matter of of this work is the study of photocatalytic semiconductors, it is necessary to introduce a brief theory of electrochemistry to describe their function. In this chapter the concepts of electrochemical reactions at semiconductor/liquid interfaces will be briefly introduced, leading to examples detailing the specifics of photocatalyst operation. This introduction is largely built upon the treatment of semiconductor electrochemistry in References [50] and [51].

5.1 Redox Chemistry

Electrochemical reactions are reactions in which electrons are transferred between chemical species during the course of their changes in bonding [50]. *Reduction* reactions are those that gain electrons from their surroundings over the course of reaction, while *oxidation* reactions lose electrons to their surroundings. Because of charge conservation, reduction and oxidation reactions occur in pairs, known as *redox* reactions. Redox reactions can occur within a localized area in solution in order to conserve electric charge, however if the electron transfer that occurs is mediated by a conducing solid or liquid the redox pair can be decoupled in space, allowing for many interesting applications.

An instructive example of electrochemistry is the voltaic cell, in which energy can be stored and released through the selective reduction and oxidation of metal species at a pair of dissimilar electrodes placed in solution [51]. For example, placing electrodes of Zn and Cu into a Cu salt solution will cause metallic Zn to oxidize and enter solution and Cu ions in the solution to reduce and deposit on the metallic electrode, according to the following reactions:

$$oxidation : \mathrm{Zn_{(s)}} \longrightarrow \mathrm{Zn^{2+}_{(aq)}} + 2\,\mathrm{e^-} \tag{5.1}$$

$$reduction : \mathrm{Cu^{2+}_{(aq)}} + 2\,\mathrm{e^-} \longrightarrow \mathrm{Cu_{(s)}} \tag{5.2}$$

One can separate the reactions in space by placing the two electrodes into separate solutions electrically linked by a salt bridge, then connecting a load across the electrodes. When a load is connected, it will see a potential difference of 1.10 V (which can be used to perform work) and the reactions will proceed until some reagent is used up (likely when all Cu^{2+} is removed from solution).

In the example above, the 1.10 V potential arises due to a 1.10 eV energy difference between energy at which $Zn_{(s)}$ will oxidize, E_{ox} and the energy at which Cu^{2+} will reduce, E_{red}. Each energy is determined empirically, as the exact energy will fluctuate with changes in the local bonding environment of each species in question. These changes can be expressed as a polarization energy

$$\Delta E_p = \gamma^2 \lambda \tag{5.3}$$

where γ is the effective charge induced on the site by polarization (giving it charge $Z \pm \gamma$ for equilibrium species charge Z) and λ is a "reorganization energy" as derived by Marcus [52]

$$\lambda = \left(\frac{q^2}{8\pi\epsilon_0 a}\right)(\kappa_{op}^{-1} - \kappa_s^{-1}) + \sum_j \frac{f_j^{ox} f_j^{red}}{f_j^{ox} + f_j^{red}} \Delta x_j^2 \tag{5.4}$$

where ϵ_0 is the permittivity of free space, a is the ionic radius, κ_{op} and κ_s are the optical and static dielectric constants of the medium, and the f's are empirical force constants for the jth bond in the system resulting from a bond displacement of Δx_j. By averaging over all possible fluctuations, it is possible to construct a function $W(E)$ indicating the probability that the energy E_{ox} or E_{red} has fluctuated to the energy E, as depicted in Figure 5.1. The midpoint between E_{red} and E_{ox} is defined as E^O_{redox}, and will be discussed later as a substitute for the Fermi energy in a solution.

The distribution of energies at which a redox half-reaction can occur partially gives rise to the concept of over-volting reaction, that is providing a potential greater than what is strictly necessary in order to drive the equilibrium reaction forward. The improvement in reactivity

by over-volting is two-fold: the redox potentials of a reaction are determined at the onset of reaction in a system, and the over-voltage allows for a greater area under the $W(E)$ curve to be accessible for reaction. As a reaction is proceeding, the system is no longer in a static equilibrium but instead in a state in which the chemical dynamics must be considered, in contrast to a simpler condensed matter physics problem in which movement of the constituent particles can be ignored.

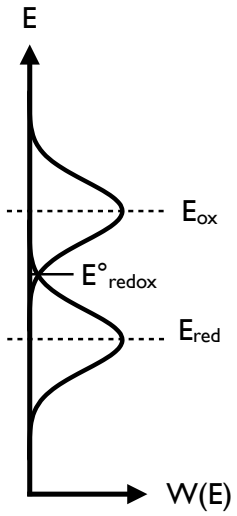

Figure 5.1: Depiction of the fluctuating energy level of a redox pair in solution. $W(E)$ represents the probability that either the oxidation energy state, E_{ox}, or the reduction energy state, E_{red}, has fluctuated from their equillibrium to energy E in response to polarization or structural changes as described by equations 5.3 and 5.4. E^0_{redox} is defined the centre point between the oxidation and reduction energies. Adapted from Morrison [50].

As is to be expected in a thermodynamic system, electrons will attempt to migrate to the lowest possible unoccupied energy state. In the case of an electron at the Fermi level of an electrode, if it has access to a oxidation or reduction site in solution then it will attempt to do so. Therefore, in the voltaic cell example above, it can be said that the Fermi level of the Zn electrode is at higher potential than E_{ox} for equation 5.1, and hence the reaction proceeds. If the Fermi level of the Zn electrode is lowered below E_{ox} by applying an external potential then the reaction will reverse.

Maintaining charge balance is an important consideration in an electrochemical reaction

and is typically satisfied on an electrode by its electrical connection to the outside world. If charge balance is not conserved and an electrode surface begins to charge, the Fermi level will move away from its equilibrium value and bend the band structure of the solid with it. An excess of electrons at the surface will bend the valence and conduction bands to higher chemical (lower binding) energy while a deficit will bend bands to lower chemical (higher binding) energy.. Without any consideration of the solid/liquid interface (which will be discussed in Section 5.3), this band bending would eventually result in a Fermi level at the same energy as the corresponding redox level, at which case the reaction could no longer proceed in the forward direction. Indeed the reaction would reach equilibrium with the electrode as any reverse reaction would reverse the charge imbalance. This limitation necessitates the pairing of redox reactions as described above.

5.2 Linking Condensed Matter Physics and Electrochemistry

The discipline of electrochemistry has a long history of describing materials (typically in solution) with respect to their electrical properties, leading to several overlapping concepts with the physics of condensed matter. By understanding the similarities between these two disciplines we can attempt to combine findings produced across both disciplines. Some of the similarities will be briefly outlined in this section.

The most notable distinction between the two fields is in the way they treat the electronic structure of a material. In physics it is usual to discuss the relative energy of electrons found in a primitive crystal cell modulated in number density by a density of states, expressed in states/eV. These states may or may not be considered as discrete levels or continuous energy bands depending on the type of system and the degree to which its electrons interact. Conversely, in electrochemistry, electrons are defined in macroscopic quantities (e.g. moles or through currents in amperes) that interact the electronic band potentials present in the system measured in volts with respect to a convenient reference frame. In a condensed matter system, energies are typically measured relative to a vacuum energy (the energy necessary to remove an electron from the solid) or to a core level that is assumed not to fluctuate

significantly during any processes the material may be subject to. By contrast, the choice of a reference corresponding to a single electron within a solid is not a convenient one to be used in an electrochemical system, instead a zero potential is defined in terms of a particular artifact, the standard hydrogen electrode (SHE).

In a standard hydrogen electrode, pure hydrogen gas at a pressure of one atmosphere flows over a platinum electrode submersed in 1 molar acid (providing 1 M of H^+ ions), and is otherwise isolated from the environment by using a mechanism through which ions may pass but oxygen is rejected (typically through enclosure in a sealed glass tube linked to solution by a salt bridge). At this electrode, the following hydrogen redox couple will establish equilibrium:

$$2\,H^+(aq) + 2\,e^- \rightarrow H_2(g) \tag{5.5}$$

After reaching equilibrium, the potential of an electron at the Pt electrode's Fermi energy is then defined to be the potential of the SHE. This potential is then used as the zero reference for other electrochemical potentials. This definition has been linked to the vacuum level through the intermediate use of the Hg work function, and is accepted to be -4.44 ± 0.02 eV [53]. Other more convenient standards have been defined that can be calibrated to the SHE, the most common of which in the material used in this study is the saturated calomel electrode.

Having linked the physical energy and electrochemical potential scales, it is worth mentioning a few additional concepts in which the two disciplines are related. While in a solid one typically considers the transport of electrons or holes through the system, electrochemical systems involve the transport of charged species through an electrolyte. These charged species complete electrical circuits by undergoing redox reactions at solvent-electrode interfaces. The inclusion of chemical reactions complicates a comparison between absolute electron energies and chemical potential as there will be a change in the free energy of a chemical species during reaction. In the case of redox reactions of simple chemical species the net changes in free energy of the pair will be quite small, especially with respect to the range of energies possible as described by the function $W(E)$. As a result of this, it is possible to define an *effective* Fermi level associated with a redox pair in solution:

$$E^0_{redox} = \frac{1}{2}(E_{ox} + E_{red}) \tag{5.6}$$

This effective Fermi level can be considered the Fermi level that will be reached by an electron in equilibrium with the two half-reactions of the redox couple with energies E_{ox} and E_{red}. This effective Fermi level could therefore be used to determine the position of the Fermi level within a semiconductor electrode that has reached equilibrium with its surroundings.

5.3 Solid/Solution Interfaces

In the interior of a crystalline solid of low-Z elements, we model the electronic states near the Fermi energy as a collection of delocalized bands in crystal momentum space that are not explicitly dependant on any particular point in space. However, electrochemistry occurs at the interface of a solid and a liquid, and we can no longer rely on the concept of an infinite repeating unit cell used to model a crystal. The introduction of the surface interface introduces many interesting physical effects that impact the electronic structure not only at the surface but within a considerable distance normal to the surface.

A discontinuous solid surface will in general lead to a non-equillibrium surface energy, as the lowest energy bonding arrangements in the interior of a solid will not necessarily be optimal at the surface. In order to minimize surface energy, thermodynamics will force the system to undergo some change in structure. There are several changes that can occur, including reconstruction of the solid surface out of the crystal structure of the bulk, ion/solvent adsorption onto the surface through either covalent bonding or weaker Van der Waals forces, and clustering of charged species

In a chemical bonding sense, one can think of the solid terminating at a surface with "dangling" bonds extending outwards into the liquid. Depending on the occupation of these dangling bonds the surface will take on a negative or positive charge. This charge can electrically polarize the region as it attracts oppositely charged species or causes polar species to align. In Figure 5.2 a solid/liquid interface is depicted along with its major features. The interface consists of three electrical *double layers*: a space charge region within the solid, the Helmholtz region of adsorbed liquid species at the solid surface, and a Gouy region that

extends further into the liquid [50]. In each double layer, the electric potential gradient will force a separation of positive and negative charge. Each charge separation will have a characteristic capacitance and thus charge will be stored, changing the electrical and chemical behaviour of the solid at its surface.

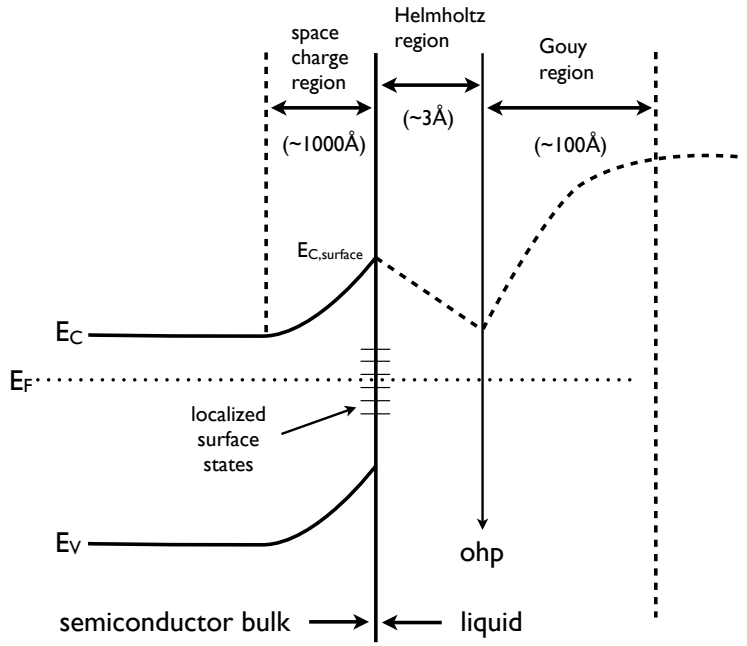

Figure 5.2: Energy diagram of a semiconductor solid/liquid interface and the changes that occur as a function of distance normal to the surface. Within the solid, a space charge region forms where majority free carriers leave the region. An n-type semiconductor with a positive surface charge is depicted, causing the bands to bend upwards in energy. This surface charge induces an opposite charged layer of solution species to adsorb on the surface, forming the Helmholtz layer. Beyond the Helmholtz layer there is a surplus of charges attracted to the surface charge forming the Gouy region. Localized surface states associated with defects are depicted, as well as the position of the outer Helmholtz plane (ohp). Adapted from Morrison [50].

The most important double layer is the Helmholtz region, which is the area with the highest stored charge per unit area. It is composed of the accumulated surface charge on the solid and the adsorbed charged species from the solution that attempts to counteract it. This region is therefore very thin and can be thought of as two planar sheets of charge. Due to the narrow separation of the two sheets, this region can accumulate an appreciable amount of charge, causing significant bending of the band structure of the material and the redox levels

of the solution. It is also in this region that electron transfer between the solid and solution is possible and redox reactions can occur. Due to the presence of the double layer the region is polarized, but the polarization is difficult to characterize due to the necessity to choose an appropriate permittivity. Neither the vacuum permittivity, ϵ_0, or the permittivity of the equilibrium solvent itself is appropriate, and hence an empirical value between the two is necessary; this limits the accuracy of our theoretical understanding of the Helmholtz region.

The other two double layers in the solid and solution arise due to the presence of the Helmholtz region sweeping away minority charge carriers in the surroundings. The Gouy region can be considered the region in which the solution holds an excess of one type of charge carrier that have been attracted by the opposite charging of the solid interface that has not been fully balanced in the Helmholtz region. The region within the semiconductor is typically known as the depletion region, and behaves similarly to the depletion region in a heterojunction, where the electric field induced by the junction sweeps mobile carriers away.

The effect of each double layer will extend on either side of the interface over a distance of many nanometres. On the liquid side, the effects will be dependant on the nature of the charged species in solution. The periodicity of the solid surface along with the electric polarization of the double layer can induce order in small charged species in the liquid as they align with surface sites. However, larger species may not be able to physically arrange themselves to counteract the solid surface charge, leading to a disordered Helmholtz region. In the interior of the solid, the difference in electron potential across the interface approximates the effect of the space charge region in a heterojunction, causing free carriers to be drawn away from the region. As a result the electronic bands for the region will bend, an effect that can extend deep within the solid (up to 1000 Å) before the effects of the surface are no longer relevant.

5.4 Redox Chemistry at a Semiconductor Surface

As electrochemical reactions must occur near an electrode surface in order for electron transfer to be facilitated, the details of the electric potential at the electrode surface are particularly important. As discussed above, interface effects where a solid and liquid containing charged

species will create a series of charged double layers at the semiconductor surface. At the actual interface, the narrow width of the Helmholtz double layer ($\approx$3 Å) will allow a large amount of charge to accumulate (since $C \sim A/d$) relative to the other layers, which can be largely ignored (also as they are not the location of surface reactions).

Because of the charge present at the Helmholtz layer, the E^0_{redox} level of a redox pair will be shifted in the vicinity of the surface. This shifting is the greatest source of uncertainty when comparing a semiconductor's bulk electronic structure to its surface structure, as the degree to which E^0_{redox} will shift depends on many factors such as the amount of charge carried on the Helmholtz layer at the time of reaction or the local environment of adsorbates and other species in the vicinity of the reaction.

Because a semiconductor contains a band gap region around the Fermi energy, the redox pair cannot come into equilibrium with the Fermi level (or vice versa) by the transfer of charge into or out of the Fermi level, as would be the case in metal. In this respect a semiconductor can be more flexible as a redox electrode, as applying an external voltage will induce a change in surface charge without it immediately conducting to the solution. This could allow the charging of a surface to be tuned to favour a particular chemical reaction pathway, for example, or to reject certain charged species from the electrode surface. In the context of a photocurrent, the ability to control surface charging in this way is particularly interesting, as an appropriate charging could induce a band transition that would not be favourable for either a hole or an electron to cross to migrate to the surface, providing a built-in method to split excitons (preventing their recombination) near the reaction site of interest.

This surface barrier voltage V_s can be determined from the charge density in the (static) depletion region, N_{dr} and the material's dielectric constant κ through the Poisson equation

$$\frac{d^2V_s}{dx^2} = \frac{qN_{dr}}{\kappa\epsilon_0} \tag{5.7}$$

which when integrated twice, choosing $x = 0$ at the surface and x_0 the boundary of the space charge region where we expect V_s to approximately equal zero, gives the result

$$V_s = \frac{qN_{dr}x_0^2}{2\kappa\epsilon_0} \tag{5.8}$$

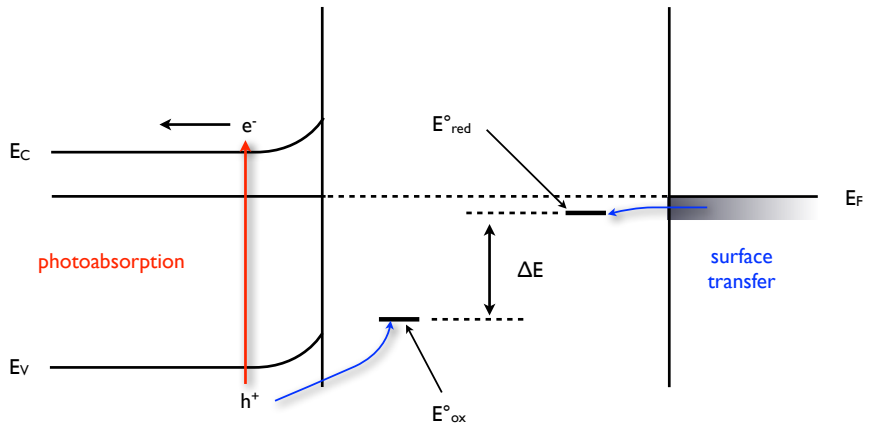

Figure 5.3: Idealized band layout of an electrochemical cell driven by a photocurrent. The two half-reactions are shown reacting at separate electrodes for clarity, however an ideal material would allow both reactions to occur within close proximity on its surface. Adapted from Morrison [50].

allowing the surface barrier to be determined from easily found physical properties of the semiconductor.

5.5 Special Considerations for Photocatalytic Redox Water Splitting on Semiconductors

To summarize the material introduced in this chapter, Figure 5.3 outlines the idealized band model of a device that could absorb photons and use their energy to perform chemical work. There are three main factors that are necessary in order for the redox reaction to be successful. First, the bands must straddle the E^0_{redox} levels of each half reaction, such that electrons can be injected to the reduction level from the conduction band via Fermi level surface states. Second, there should be sufficient surface barrier voltage resulting such that carrier recombination is minimized. Third, there should be sufficient overvoltage such that competing redox reactions (such as electrode corrosion) do not compete with the desired reaction, but not too much overvoltage that significant energy is lost to heat or to cause the material to be unable absorb light from solar spectrum in the first place.

To date, the choice of materials to meet these requirements has been quite limited. When photocatalysis was first being investigated in the 1970's very few materials even met

the first criterion [54, 55]. Metal oxides such as TiO_2 and ZnO had the appropriate band positions, however their band gaps were too high to use visible light. Compound systems could theoretically be assembled from two materials with band edges suitable for each of the half reactions, however these systems would lose further energy to the built-in contact voltage drops necessary to connect them [56]. Because empirical techniques are typically required to determine the band edge positions of a solid in solution the ability to rapidly test new materials was hampered and the field lost interest for a number of years. However, further research has revealed opportunities to create the appropriate band structure in new materials and with sufficient understanding a practical water splitting photocatalyst may be found.

Chapter 6

Gallium nitride:Zinc Oxide photocatalyst

6.1 Photocatalytic activity of ZnO

While several transition metal oxides have an appropriate conduction band energy to photoreduce H_2 gas from water, ZnO is particularly resistant to corrosion during the process, making it a good candidate for applied use. ZnO is insoluable in water, and it is synthesized in large quantities at low cost owing to its elemental abundance and its many industrial applications. It has therefore attracted interest in the past as a material to be optimized for photocatalytic use, especially as a means of decomposing organic pollutants such as cyanide, phenols and chlorinated hydrocarbons [57–59].

The primary limitation to ZnO as a practical photocatalyst for large-scale hydrogen production is its high band gap of 3.3 eV, which only permits it to absorb in the UV portion of the solar spectrum. If the band gap of ZnO could be sufficiently decreased without impacting the intrinsic properties that make it a good UV photocatalyst then a viable material for water splitting might be realized.

There have been several attempts to do reduce ZnO's band gap by introducing new states into the valence band to increase its onset energy. One strategy to narrow the band gap of ZnO is to substitute O *2p* electrons, which comprise the valence band maximum, with higher energy electrons. This can be achieved by substituting oxygen for other elements in its period, such as the complete substitution of sulphur in ZnS [60] or partial substitution of Se in $ZnO_{1-x}Se_x$ [61],

The ZnO valence band is characterized by a narrow band of O *2p* states at higher orbital energy with a narrow band of Zn *3d* / O *2p* hybridized states below it, as depicted in Figure 6.1.

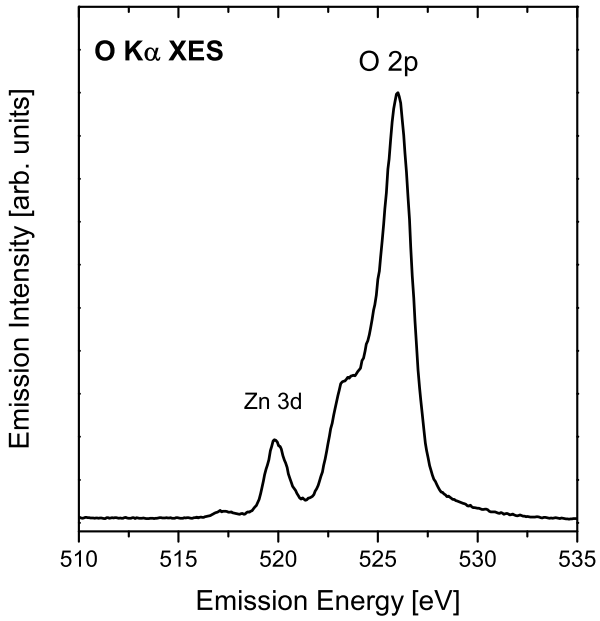

Figure 6.1: X-ray Emission spectra of the valence band of powdered ZnO. The O *2p* states are pushed into a narrow band by the presence of Zn *3d* states, however coupling between these states causes complications in treating the system using DFT [62]. The feature below the Zn *3d* band is second order Zn L_2 emission.

Substituting Cd for Zn has been attempted in systems such as CdSe and $Cd_xZn_{1-x}Se$ but the resulting powders were found to show low activity as particle surface area increased and the material dissociating under illumination [63]. The deep Zn *3d* band in ZnO appears to be fully disconnected from the O *2p* band, so subtle modification of its position in energy could control the position of the O *2p* band by state repulsion. This is likely the mechanism that would cause a decrease in the band gap with Cd substitution, as Cd 4d electrons would have a higher orbital energy and repel the O *2p* band edge to higher energy, though this process may be complicated by the bands connecting.

6.2 GaN:ZnO solid solution

In this work we investigate a substitutional solid solution of GaN with ZnO (which will be referred to as GaN:ZnO or $(Ga_{1-x}Zn_x)(N_{1-x}O_x)$), which is the first successful example of overall water splitting using a visible-light absorbing photocatalyst [7]. GaN:ZnO shows a

0.6 to 0.8 eV decrease in band gap from either precursor, making it an interesting case of band gap engineering. The reduced band gap allows for an increase of the absorption from the solar spectrum and an improved photocatalytic activity.

In collaboration with fellow graduate students Teak Boyko and Robert Green, three samples of $(Ga_{1-x}Zn_x)(N_{1-x}O_x)$ with compositions $x = 0.06, 0.18$ and 0.42 were measured. XES and XAS measurements were acquired at the ALS Beamline 8.0.1 and CLS SGM, respectively, as previously reported [16].

While the decreased band gap of GaN:ZnO had been previously characterized by UV/vis reflectance, there was a great deal of uncertainty in the literature as to the mechanism for this decrease. Additionally, it had been assumed that the material could be structurally described as a single phase of oxynitride material, where Ga and Zn were bonded to both N and O throughout the system. An example of this oxynitride super-lattice structure can be seen in Figure 6.2 which is derived from a structure presented by Jensen *et al.*[62].

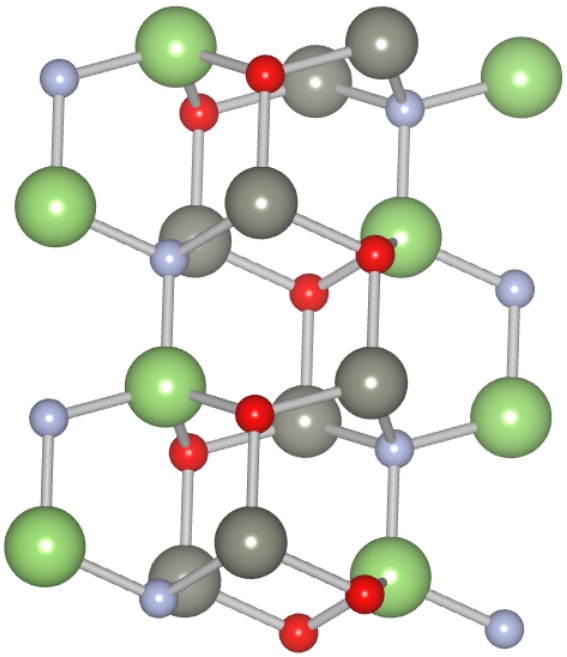

Figure 6.2: 32 atom supercell of a GaN:ZnO structure proposed by Jensen *et al.* [62]. The structure was force optimized without enforcing cell symmetry. Both Ga and Zn (green and grey) are bonded to O and N (red and blue) in equal number, and is referred to below as the oxynitride superlattice structure of GaN:ZnO.

Table 6.1: Preparation conditions for $(Ga_{1-x}Zn_x)(N_{1-x}O_x)$ samples

Sample	Initial Zn/Ga ratio	Temperature (K)	Time (h)	x
GAZN42	1.0	1223	0.5	0.42
GAZN18	1.0	1123	12	0.18
GAZN06	1.0	1123	50	0.06

GaN and ZnO both share the same wurtzite crystal structure with similar unit cell dimensions (GaN: a = b = 0.319, c = 0.519 nm; ZnO: a = b = 0.325, c = 0.521 nm) [64]. Additionally, both ZnO and GaN are d^{10} metal cation systems, giving them similar electronic and bonding structure. The similarity of their structures allows a solid solution of both materials to form through Ga/Zn and O/N substitution without inflicting a substantial interface energy penalty between phases and without changing the crystal structure or significantly affecting the lattice parameters of the precursorsz. The similarity of the two precursor materials appear to offer the possibility of producing a Zn oxynitride material with both the photocatalytic properties of ZnO and a lower band gap caused by N *2p* states to raise the valence band maximum and close the high band gap.

The GaN:ZnO samples we worked with were synthesized by Maeda *et al.* from a physical mixture of $\alpha-Ga_2O_3$ and ZnO derived from commercial sources [7, 16]. This physical mixture was heated to high temperature (greater than 1123 K) at a rate of 10 K/min and then nitridated with an NH_3 flow (250 mL/min) [65]. Preparation temperatures and molar ratios are summarized in Table 6.1.

Maeda and Domen demonstrated that GaN:ZnO shows a maximum photoactivity at a pH of 3.0[66]. At lower pH it is expected that surface metal sites will begin to dissociate from the material and enter solution, but the change in activity with pH shows that the electronic band bending at the surface (as described in section 5.3 is an important factor to optimize in this material. Maeda *et al.* have experimented with depositing nanocrystalline co-catalysts on the surface as a means of increasing activity, but these have typically been rare-earth metals that would drive up the cost of a material desired for mass production. Further study of the solid/solution interface of GaN:ZnO is warranted and may lead to further improvements in

performance without the need to resort to rare-earths.

What had not been clear before this study was the mechanism behind GaN:ZnO's reduced band gap as compared to ZnO. DFT calculations have been performed by several authors [62, 67–71], all of whom carefully considered the problem of GaN:ZnO band gap reduction using various structural models of a single-phase oxynitride system that displayed reduction of the band gap. However, DFT calculations typically underestimate the band gap in wide band gap semiconductors [25]. Additionally, simple DFT calculations underestimate the ZnO band gap by 75% and are complicated by the treatment of oxygen vacancies [72]. Therefore, comparing a calculated band gap with experimental results was a poor metric that could be expanded upon using our X-ray measurements of the valence and conduction band structure.

6.3 Binding energy picture of GaN:ZnO

In order to better understand the band gap behaviour of GaN:ZnO, it is necessary to determine band onsets for the valence and conduction bands. This can be accomplished using X-ray emission and absorption spectroscopy, respectively. Because these methods involve an elementally specific core-level transition to the valence or conduction band, it is not immediately apparent which element valence band emission will begin at the highest absolute electron energy, or which element begins absorbing at lowest conduction band energy. Because each X-ray spectra is measured relative to a chosen core energy, it may be necessary to convert these measurements to a common binding energy scale before interpretation is possible.

The GaN:ZnO system was particularly challenging to interpret due to a peculiar feature: a facile interpretation of O and N K-edge spectra produced two separate possible band gaps for the system, with the N K spectra displaying a 2.6 eV gap and O K spectra separated by 4.4 eV. This behaviour of two energy gaps should not be possible for a material with a single material phase. Given that all prior theoretical predictions of the electronic structure of GaN:ZnO suggested that the valence band consisted of hybridized O and N *2p* states at the top of the valence band, a finding of two band gaps that varied depending on the element measured is not expected. In order to determine whether the O and N *2p* states separated

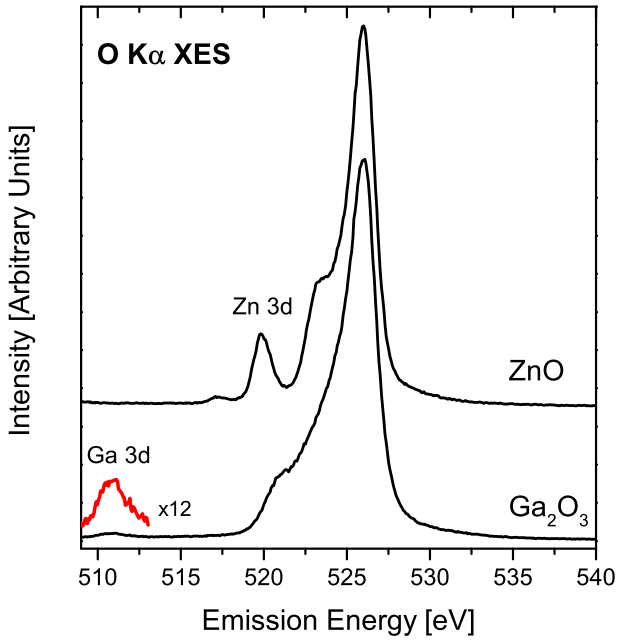

Figure 6.3: Comparison of Oxygen Kα XES of ZnO and Ga_2O_3. Hybridization of oxygen *2p* states with *3d* states from each material's metal centre can be observed, providing an indication of the relative binding energy of these metal states. Ga *3d* states are enlarged for clarity.

in the valence band, it was necessary to determine the relative offset between these XES measurements and build a binding energy alignment of the measurements.

O Kα XES measurements of Ga_2O_3 show a faint feature just above 510 eV, as depicted in Figure 6.3, that is indicative of Ga *3d* - O *2p* hybridization [47]. There is no similar feature at this energy in ZnO, allowing us to use this as a fingerprint of Ga *3d* states in the material. These states are located significantly below the valence band (by over 15 eV) and so should behave as semicore states within the material. It is therefore reasonable to assume that these states will not change significantly with the valence chemistry of the system, and should remain at approximately the same binding energy in GaN:ZnO. Because of this insensitivity, it is possible to use the Ga *3d* feature as an anchor point in binding energy, allowing one to align spectra in energy so long as this feature is detectable within them. The peak energy position of this feature did not appear to shift over the different concentrations of O in the GaN:ZnO samples, though it is does decrease in intensity making it difficult to differentiate

from noise in the measurement.

The Ga *3d* feature is also visible in our N Kα spectra of GaN [73] and GaN:ZnO, and so by aligning this feature on a common axis with the Ga *3d* - O *2p* hybridization, it is possible to align these spectra, as depicted in Figure 6.4. Calibration of each XES spectrum in this diagram are made with respect to reference samples listed in Table A.1. This figure shows the measurements for sample GAZN42 which had the least Ga/N content of the measured spectra. We can also align our Zn L_3 XES measurements with the O Kα spectra by using a binding energy offset of 490.9 eV derived from XPS measurements for $(Ga_{1-x}Zn_x)(N_{1-x}O_x)$ at $x \leq 0.15$ [74]. While the Ga L_3 XES spectrum was measured, it does contain interesting features, nor does it correspond to the valence band, so it is emitted from this binding energy picture.

Once the constituents of the valence band are aligned in this fashion, several observations can be made that support the choice of alignment. First, in the O Kα spectrum, the Zn *3d* - O *2p* hybridization feature below the valence band (labelled C') aligns with the Zn L_3 spectrum (labelled C), indicating the offset of 490.9 eV from the core binding energies is a good match (the difference in energy between peaks C and C' is again 490.9 ± 0.1 eV). Second, magnifying the high-energy side of the Zn L_3 spectrum shows a small feature (labelled B) that aligns with the main peak of the O spectrum. There is an additional bump that appears to align with the main peak of the N spectrum, however it is indistinguishable from noise if the background slope is subtracted, and so is not used as further evidence of alignment.

A third piece of evidence that supports the proposed energy alignment is the position of the Zn *3d* - N *2p* hybridization peak (labelled C"). While relatively weak, this feature does become more intense as more Zn is introduced into the system. This increase in intensity is displayed in more detail in Figure 6.5. The alignment of peak C" with C and C' indicates that the Ga *3d* state alignment has brought the N Kα XES spectrum in good alignment with the O Kα and Zn L_3 spectra despite not being offset by an XPS binding energy difference (no single XPS offset energy was available to use as alignment).

It is possible to introduce conduction band information into this binding energy picture by including the O *1s* and N *1s* XAS spectra. These spectra can be easily aligned to their respective XES spectra as they are measured with respect to the same *1s* core state. The

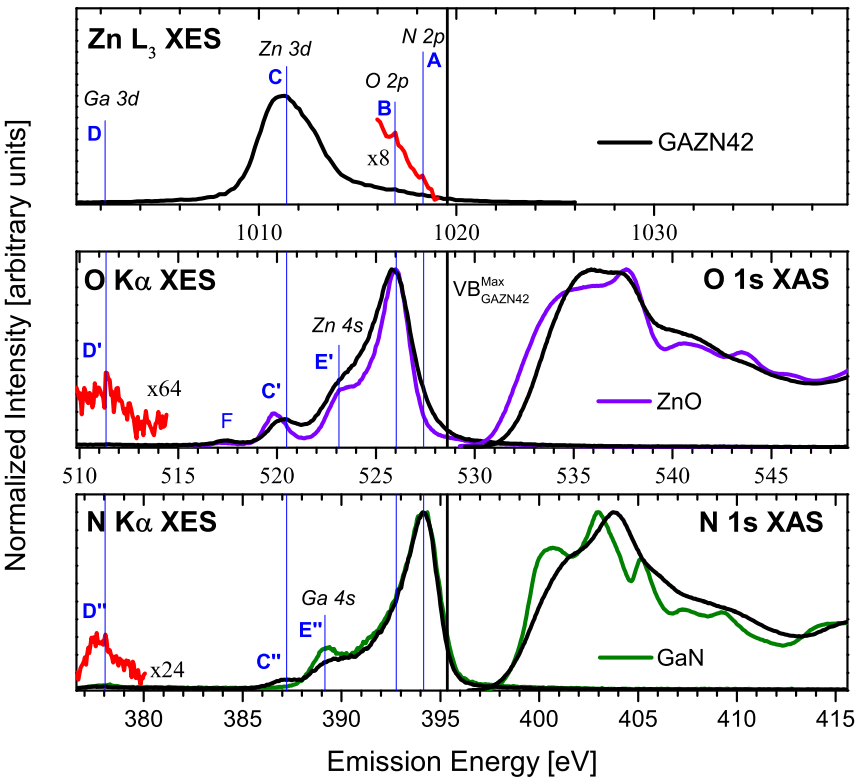

Figure 6.4: Comparison of Zn L_3, O Kα, and N Kα XES of $(Ga_{1-x}Zn_x)(N_{1-x}O_x)$ at $x = 0.42$ (sample GAZN42). The precursor materials, GaN and ZnO, are also plotted for comparison. The spectra have been aligned to demonstrate hybridization of Zn states (labeled C, C',C") and Ga states (D' and D") with the N and O *2p* states. This allows us to consider the relative binding energy of all near-Fermi level states. Peak F is second order Zn L_2 emission and does not represent O DOS.

measured XAS spectra are calibrated to known standards listed in Table A.2. It would normally be necessary to adjust the position of these XAS spectra upwards in energy by a small amount to compensate for the core hole effect (discussed in section 4.3). However, a WIEN2k calculation of a 2x2x2 GaN supercell including a core hole shows a downward shift in conduction band DOS but no shift of the onset energy, suggesting that the N *1s* XAS measurement should be relatively unaffected by the core hole in that GaN:ZnO measurements.

With the binding picture of sample GAZN42 composed in this manner, it is now possible to determine which states contribute to the valence band maximum and conduction band minimums. In both cases, it is N *2p* states that are extending furthest into the band gap, indicating that N participates more than O in the vicinity of the band gap. The surprising

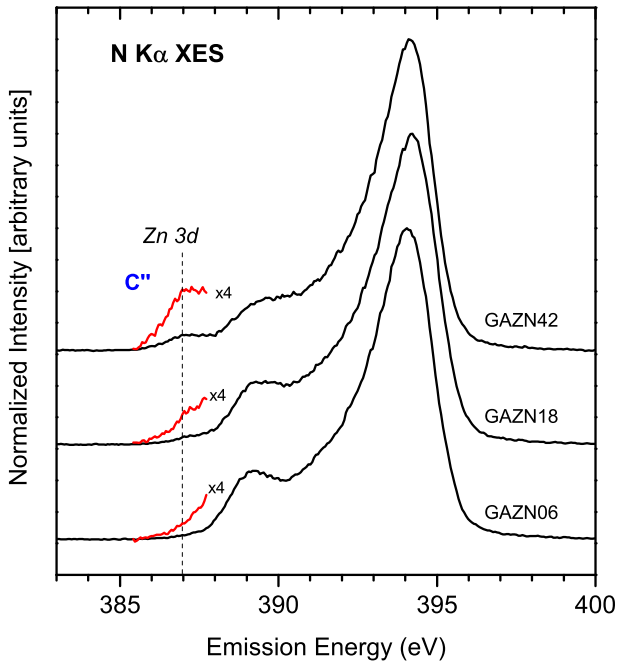

Figure 6.5: Comparison of N Kα XES for $(Ga_{1-x}Zn_x)(N_{1-x}O_x)$ for $x = 0.06 \rightarrow 0.42$. The intensity of the Zn *3d* contribution (labelled C") increases with increasing Zn concentration and becomes a distinct peak at higher concentrations.

result is that the edges of the O measurements fall appreciably further from the band gap. This result seems to contradict the premise that GaN:ZnO is behaving as a single material, as such a system should only be capable of having one band gap, even if the states that comprise the edge of the gap do not receive a contribution form all atoms in the structure.

6.4 GaN:ZnO DFT simulation

As mentioned above, several DFT models of the GaN:ZnO system exist in the literature [62, 67–71] as a starting point for analysis of our XES and XAS measurements. However, it was desirable to recreate some of this work to investigate two factors: the degree to which O and N *2p* states hybridized in the valence band (and by extension would be expressed in the XES measurements), and to investigate the degree that the valence band structure would be controlled by adjusting the Coulomb parameter (U) in the GGA+U exchange functional [75, 76].

Table 6.2: Bond lengths of model GaN:ZnO structures

Model	Bond	Bond length (Å)
$x = 0.5, 0.4375$	Ga $\rightarrow$ N	1.959
	Ga $\rightarrow$ O	2.010
	Zn $\rightarrow$ N	2.010
	Zn $\rightarrow$ O	1.919
$x \rightarrow 0$	Ga $\rightarrow$ N	$1.951 - 1.990$
	Ga $\rightarrow$ O	$2.060 - 2.074$

Two structural models were chosen to simulate the extremes of $(Ga_{1-x}Zn_x)(N_{1-x}O_x)$ composition measured. A 32 atom structure with $x = 0.5$ was available from Jensen *et al.* with 8 O and 8 N [62] to represent an oxynitride supercell structure (although Jensen's structure has striped ordering of the N and O sties). From this structure, a 2x2x1 supercell was constructed with two N substituted for O, giving 18 N and 14 O, giving $x = 0.4375$. This structure was used in order to examine the effect a slight deviation from an equal amount of O and N. At the other extreme of concentration, Yoshida *et al.* had examined 108 atom supercells of GaN with single Zn and O defects substituted in an attempt to study the marginal effect of dilute ZnO in a GaN host [71]. All three structures were force-relaxed with WIEN2k after modification, and the optimized structures are displayed in Figure 6.6. The range of bond lengths in the optimized are provided in Table 6.2. As these structures had already been well investigated and existed in the literature, we did not want to complicate matters by using additional structural candidates. These structures used also proved sufficient to explain the observations, as will be discussed below.

Structures for GaN and ZnO were retrieved from the Crystallography Open Database for comparison with the solid solution structures. The structures used were originally compiled by Wyckoff[77].

The WIEN2k code was used to calculate the electronic structure of each structure using the PBE-96 GGA functional [78]. A Hubbard potential ()$U = 7.5\,\text{eV}$) was applied to the *3d* orbitals of Ga and Zn in order to place these states at the correct energy with respect

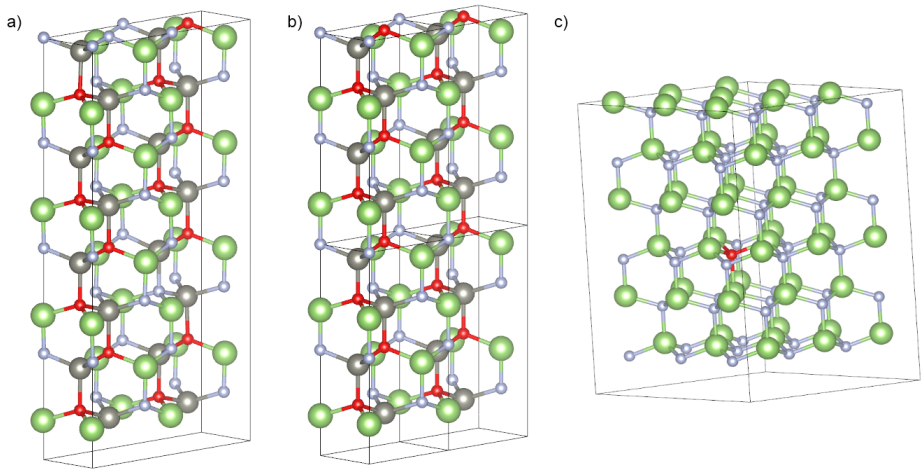

Figure 6.6: Structures used to model $(Ga_{1-x}Zn_x)(N_{1-x}O_x)$ for $x = 0.5$ (a), $x = 0.4375$ (b) and $x \to 0$ (c). Model (a) is derived from Jensen *et al.* [62], Model (b) is Model (a) with two N sites substituted with O and Model (c) was derived from Yoshida *et al.* [71]. Ga is shown in green, Zn in grey, N in blue and O in red. Calculated X-ray emission spectra of each model are presented in Figure 6.7.

to *2p* states in the valence band. This value of U was arrived at by meeting two criteria: it should be similar in value to the 7 eV used by Huda *et al.*[67] and it should approximately reproduce the *2p-3d* peak splitting in our ZnO XES measurements (these proved to show better agreement than the *2p-3d* splitting in our GaN calculations). WIEN2k was instructed to generate 1000 k-points for each crystal structure in order to ensure a sufficiently dense k-point grid was used for all structures despite their varying unit cell volume. This choice of k-points proved sufficient for good convergence of the set of structures after testing several of the structures with greater and fewer k-points.

As WIEN2k includes the core electrons of each atomic site in its converged basis set, calculations of each structure were repeated with a *1s* core hole introduced into a single N or O site in order to simulate a core-hole excitation of the ground state system. In each case a background electron was added to the system in order to maintain charge balance. For the small unit cell structures (ZnO and GaN) a 2x2x2 supercell was used to isolate the core-hole atoms from each other, however this seemed unnecessary in the larger structures. There was some difficulty in converging the O core holes in the oxynitride supercell structures, however

the experimental results showing N *2p* states at the conduction band minimum allowed these cases to be ignored. The GaN core-hole structure was found to have no difference in conduction band onset, and so it was assumed that all N *1s* XAS measurements accurately represented the onset of conduction band states within the measurement error of ±0.1 eV.

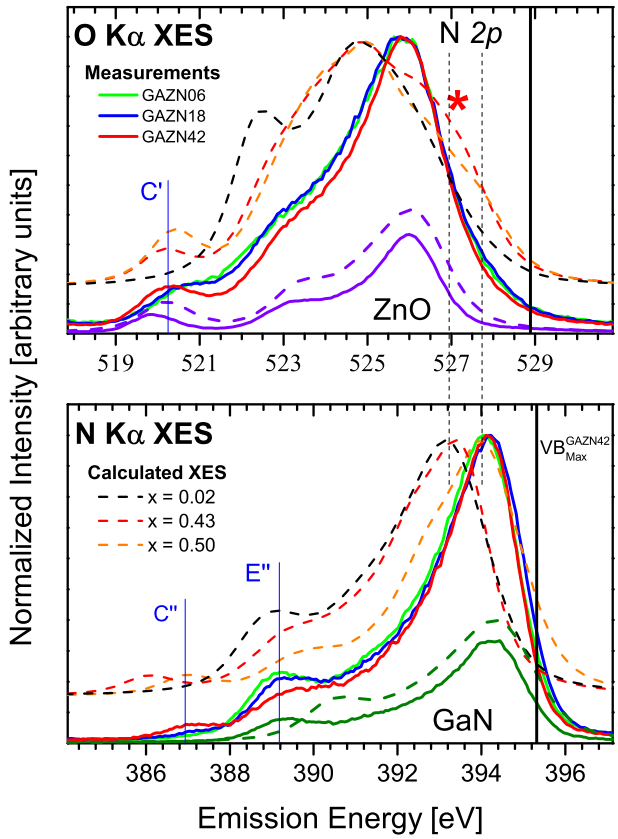

Figure 6.7: Calculated X-ray emission spectra (dashed lines) versus experimental measurements (solid lines). The calculated spectra predict a shoulder (marked with an asterisk) on the high-energy side of the O Kα peak from hybridization with N *2p* states, as well as increased repulsion of the N Kα peak to higher energy with increasing O composition. Neither effect is observed in the experimental measurements; instead the primary peak of the GaN:ZnO XES measurements most closely resemble pure GaN and ZnO, confirming GaN:ZnO behaves as a heterojunction solid solution of GaN and ZnO (reference spectra and calculation stacked beneath for comparison).

Once a self-consistent set of wave functions were computed with WIEN2k, it was trivial to project them as a density of states (DOS) for rough comparison with our experimental measurements. Using a DOS projection, each solid solution's states was aligned by the Ga

3d state peak in order to plot them on a common energy scale (WIEN2k uses a somewhat arbitrary energy scale by default). The DOS alignment could subsequently be used to align calculated XES spectra created with the XSPEC code included with WIEN2k. This relative alignment was particularly important for aligning the $x \to 0$ calculated O K XES, as it does not have any Zn states and the Ga-O hybridization was negligible. The calculated N and O K XES is compared to the experimental measurements (Figure 6.7).

Two important results can be drawn from the calculated XES spectra. The first is that the calculation predicts the N K XES peak should shift upwards in energy with increasing O concentration (as x increases). This result is not surprising, as the calculation places the bulk of the O *2p* states at lower orbital energy than the majority of the N *2p* states. This ordering of N *2p* states above O *2p* states is confirmed by the binding energy picture of GaN:ZnO that was built from our XES measurements. As a mechanism do explain the shift, one can surmise that the introduction of O *2p* states into the centre of the valence band would repel the N *2p* states above it to higher energy [79], as confirmed by the calculation. However, in the XES measurements, there is no discernible energy shift of the N K XES spectrum between samples, which indicates that state repulsion does not occurring between the O and N *2p* states.

The second notable result of the calculation is that it predicts the O K emission spectrum to have a shoulder on its high energy side that results from hybridization of the O *2p* states with N *2p* states. This shoulder is predicted to increase in intensity as the relative ratio of O to N stoichiometry in the material changes; of the sample concentrations calculated the hybridization feature is sharpest and of highest intensity at $x = 0.4375$. However, in contradiction to the calculated results, this feature is entirely absent from the O K emission spectra. There is a small difference in broadening between the O peaks depending on the sample being measured, but these are likely due to differences in crystallinity between the samples rather than any O hybridization.

These disagreements between the calculated model and the actual measurements indicates that an oxynitride crystal structure with long-range ordering is not being measured. While Zn-N and Ga-O bonding does occur in the system (indeed, the alignment of the binding model in Figure 6.4 depends on this), the necessary equivalence of O and N sites in the structure does not exist and the O and N *2p* states do not hybridize to the degree that they would if

the DFT test models were correct. This disagreement of the models with experiment also resolves the issue of the apparent multiple band edges in the experimental binding energy picture. If the experimental results cannot be described by a single ordered structural model, then it indicates the materials are not homogeneous at the length scale at which the O and N state hybridization can occur. The solid solution is therefore not truly homogeneous and a better model to describe its electronic structure should be considered.

6.5 GaN:ZnO as a Heterojunction Solid Solution

If GaN:ZnO is composed of two or more crystalline phases then what can the binding energy picture in Figure 6.4 tell us about the material's behaviour? Previous XRD studies of the material conclude that a solid solution with lattice parameters between GaN and ZnO is present in the GaN:ZnO samples, approaching the used in the above DFT calculations as the nitrogen to oxygen ratio approaches 1:1 [7]. For example, Figure 6.8, presented in Reference [7], shows three features characteristic of the wurtzite crystal structure for GaN, ZnO and $(Ga_{1-x}Zn_x)(N_{1-x}O_x)$ between $x = 0.22$ and $x = 0.05$ (plots a - e). The progression from no nitridation to complete nitrogen can be observed as the peaks shifting from low to high θ, and this suggests that the intermediate measurements are of strained wurtzite crystal structures with cell parameters between ZnO and GaN. From this observation it was concluded that nitridation of the Ga_2O_3/ZnO mixed powder precursor formed a single wurtzite phase with reduced band gap.

Since the binding energy picture of the GaN:ZnO discounts the existence of a single oxynitride phase with long range ordering, the XRD result must instead describe multiple crystal phases, perhaps a range of them. The intermediate material peaks highlighted in Figure 6.8 are overlap in angle the GaN and ZnO precursor powder measurements, wide enough that the position of GaN and ZnO peak maxima are beneath the GaN:ZnO peaks. This suggests that the intermediate XRD measurements could be describing a summation of the precursor phases rather than a single phase. However, the XRD peak has only a single maximum, so it cannot be a summation of pure precursor crystal structures. Instead it would be a summation over a range of crystal phases under some distribution of interface strain.

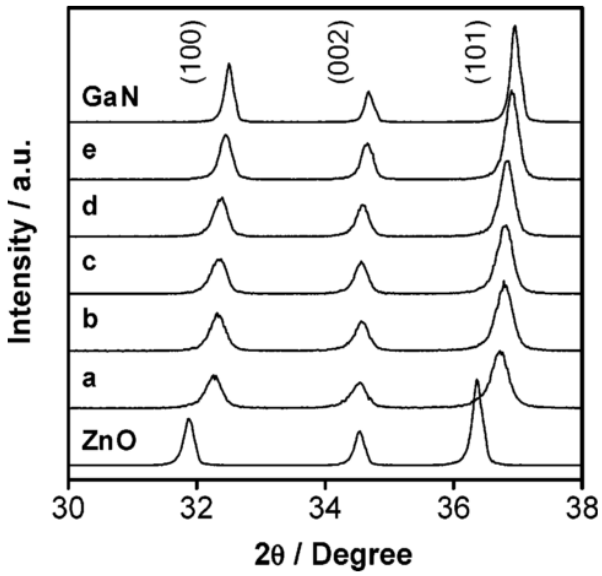

Figure 6.8: XRD measurements of GaN, ZnO and several GaN:ZnO intermediates. The plot most similar to the compositions investigated in this work are plots a ($x = 0.22$), b ($x = 0.17$) and d ($x = 0.10$). Maeda interpreted the intermediate measurements as consisting of a single wurtzite phase, however the broadening of the each peak could also be interpreted as a combination of strained ZnO and GaN phases being measured simultaneously, as the peak width is sufficient to encompass the GaN and ZnO peak positions. Reproduced from Ref. [7]

This suggests that the region of interest in GaN:ZnO is in fact an *interface* between GaN and ZnO phases rather than an independent crystal structure that can be isolated and studied independently of the two precursors.

The nature of this more complex mixture of GaN and ZnO phases hav been investigated by Li *et al.*, who built a model of GaN:ZnO formation dynamics using a Monte Carlo method [80]. This model predicted that at elevated formation temperature a disordered phase structure would occur. At $x = 0.5$ the phase transition temperature is 870 K, and at $x = 0.25$ it reduces to 760 K, both well below the formation temperature of the sample measured in this work. By taking snapshots of their model, such as the slices show in Figure 6.9 Li was able to demonstrate that GaN and ZnO will preferentially cluster together in random formations. Li's modelling predicts that an ordered oxynitride state should exist at concentrations approaching $x = 0.5$ but that it should be barely stabilized compared to the phase separated form (by

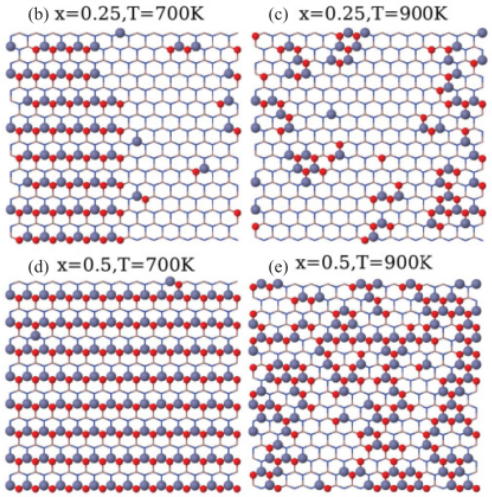

Figure 6.9: 14x1x8 unit cell slice of various GaN:ZnO structures calculated by Monte Carlo simulation under conditions below (b,d) and above (c,e) the phase transition temperature for each concentration x. O is shown as small red circles and Zn as larger blue circles, with Ga and N hidden. Below the phase transition temperature, GaN:ZnO forms an order oxynitride lattice structure, however above it the material forms disorderd phases of separate GaN and ZnO. Reproduced from Ref. [80].

about 3 meV per atom). The highest ZnO concentration of our measured samples is $x = 0.42$, outside Li's prediction for the ordered phase concentration, so the assumption above of a mixed solution of GaN and ZnO would be favoured.

Disordered versus superlattice alloying of GaN and ZnO have been theoretically investigated using DFT by Huda *et al.*, who found that both order and disordered structural models could achieve the reduced band gaps observed in experiments [67]. However, the overall absorption coefficient of the disorderd structure was calculated to be superior to the superlattice system, a result that was attributed to increased spatial overlap of valence band and conduction band orbitals as phases of each material were brought into contact (Huda's superlattice model required thick layers of GaN and ZnO in order to reproduce the experimental band gap). Huda also investigated various structural models of the interface itself, finding that an interface wih a minimum number of Ga-O and Zn-N bonds was favourable. As with the findings discussed above, these results suggest that the interface between separate GaN and ZnO phases is responsible for the decreased band gap and optical absorption of the GaN:ZnO sysem.

Returning to our experimental results, the similarity between the majority of *2p* states in the O K XES measurements of GaN:ZnO and ZnO and the N K XES measurements of GaN suggests that ZnO and GaN phases are quite similar to those isolated precusors in the vicinity of the band gap. The band edges in GaN:ZnO instead seem to simply be slightly broader and shifted in energy to produce a reduced band gap. This behaviour can be attributed to band bending along phase interfaces, a feature consistent with a solid state heterojunction interface. Across such an interface one expects the Fermi energy to remain constant but the valence and conduction band edges to bend between the intrinsic edges of each phase and to connect. The connection allows charges to cross the junction without significant scattering as long as they have sufficient energy, which would facilitate the seperation of exciton pairs, as will be discussed below.

Further evidence of the separation of chemically distinct phases within GaN:ZnO is obtained by examining O *1s* TEY vs TFY measurements as shown in Figure 6.10. Features α and γ can be considered indicitive of Ga bound O in the solid solution, while feature β is unique to Zn bound O. As the samples undergo nitridation, excess ZnO will be eliminated from the solution, causing feature β to be extinguished while feature α grows. From feature α it appears that Ga_2O_3 takes over as the primary oxygen species at low Zn content, but for samples GAZN42 and GAZN18 the remaining spectral weight under feature β indicates that ZnO-like O remains present in the bulk. However, on the surface in the TEY measurement, feature β' is largely extinguished even in GAZN42, while feature γ' is more pronounced, indicating that the surface oxide layer is primarily Ga_2O_3. This surface Ga_2O_3 is not surprising, as its cubic crystal structure would likely be rejected from the solid solution due to lattice mismatches. The overall picture is that of a solid solution of ZnO phases contained within a GaN host.

Proceeding with the model of GaN:ZnO as a non-homogeneous solid solution with and considering the regions between predominantly ZnO and predominantly GaN composition as heterojunctions, we can now attempt to extract the band offsets between the two phases of the material to arrive at a band gap. As was shown in Figure 6.4, the N *1s* XAS onset is at lower binding than the O *1s* onset, so if we are searching for the lowest possible band gap it is sufficient to consider only the negligible core hole shift of the N conduction band and ignore the shifting of the O CB. A detailed view of the band gap region is show in Figure

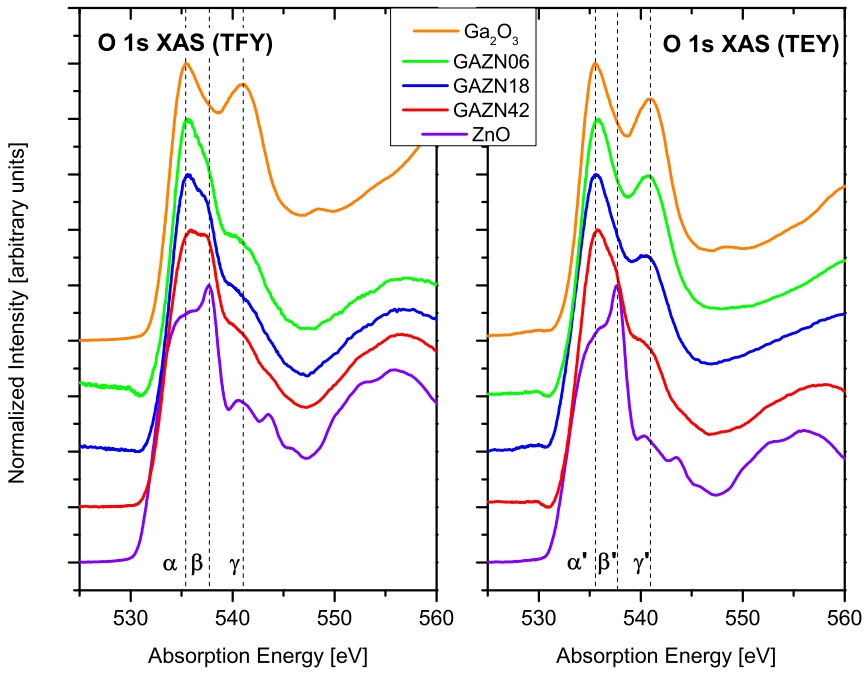

Figure 6.10: O *1s* XAS total fluorescence yield (TFY) peak β indicates the contribution of ZnO-like O conduction band states within the sample at $x = 0.42$. This contribution is reduced with decreasing x. This is in contrast to the O *1s* XAS total electron yield peak γ', which indicates the dominance of Ga-O bonding on the surface of the GaN:ZnO samples.

6.11 for the O and N measurements, using the same alignment as used above, but for each of the sample concentrations measured. As can be seen, the valence band maximum for each phase is relatively unchanged with concentration (apart from some minor broadening differences due to the normalization). The conduction band minimum, however, decreases with increasing ZnO concentration (x) in both the O and N XAS. Therefore it is immediately clear that the band gap closes from the conduction band with increasing x. Additionally, the N conduction band edge is offset slightly below the O edge, by about 0.2 eV. As the N valence band maximum is clearly higher than the O (due to the higher N *2p* orbital energy) we can say that the minimum band gap will occur in the GaN phase of the solid solution.

ZnO and GaN are plotted for comparison in Figure 6.4 and provide an interesting challenge to the above finding of N states at the conduction band minimum: ZnO intrinsically has a lower conduction band edge. This indicates that in solution the ZnO band edge has been

forced to higher orbital energy by the presence of the majority GaN phase, likely as a result of a greater number of unoccupied N *2p* states at low energy in the precursor materials. GaN displays an absorption feature that peaks slightly below 400 eV, whereas ZnO's feature occurs about 1.5 eV higher (with respect to a non-existant N *1s* core level in this binding energy alignment). As the GaN feature is at lower energy and GaN is the majority phase of the samples we measured, these unoccupied states repell the ZnO states to higher energy.

In order to determine the relative band offsets we need a metric to choose a single position in energy to the broad decay of an emission or absorption spectrum. As discussed above, a number of effects including experimental considerations, such as the bandwidth of the exciting X-ray beam or imperfections inherent to crystal gratings, and inescapable quantum mechanical effects, such as the short core-hole lifetime combined with the uncertainty relation between energy and time, result in spectral broadening. Our research group has found that this broadening can be circumvented by using positive second derivative peaks to determine the regions "under" the spectrum corresponding to the rapid onset of states [81]. Using second derivatives to determine band gaps has been shown to produce good agreement with various materials such as the post-transition metal oxides [47]. As a result, the positive second derivative of each spectrum is plotted, and offsets between relavent features can be found in Table 6.3.

Given the above analysis, we also propose a mechanism to explain the decrease of GaN:ZnO's band gap with increasing ZnO concentration. Because the ZnO conduction band edge has been forced above the GaN onset, an increase in ZnO states should in return repell the GaN onset downwards in energy. Over the sample concentrations measured this repulsion causes a 0.4 eV decrease in the minimum band gap energy from low to high ZnO concentration ($x = 0.05 \rightarrow 0.42$). However, assuming phase separation within the solution, other gap transitions should be possible, such as from the GaN valence band maximum to the ZnO minimum (which may be experimentally observed in photoluminescent experiments [71]). Higher energy transitions initiated from the ZnO valence band maximum would be of little interest in a photocatalytic system as they would occur above 4 eV.

The overall result of our GaN:ZnO analysis is that the material has an energy gap of 2.6 eV associated with the GaN host phase and a 2.8 eV gap associated with the minority ZnO

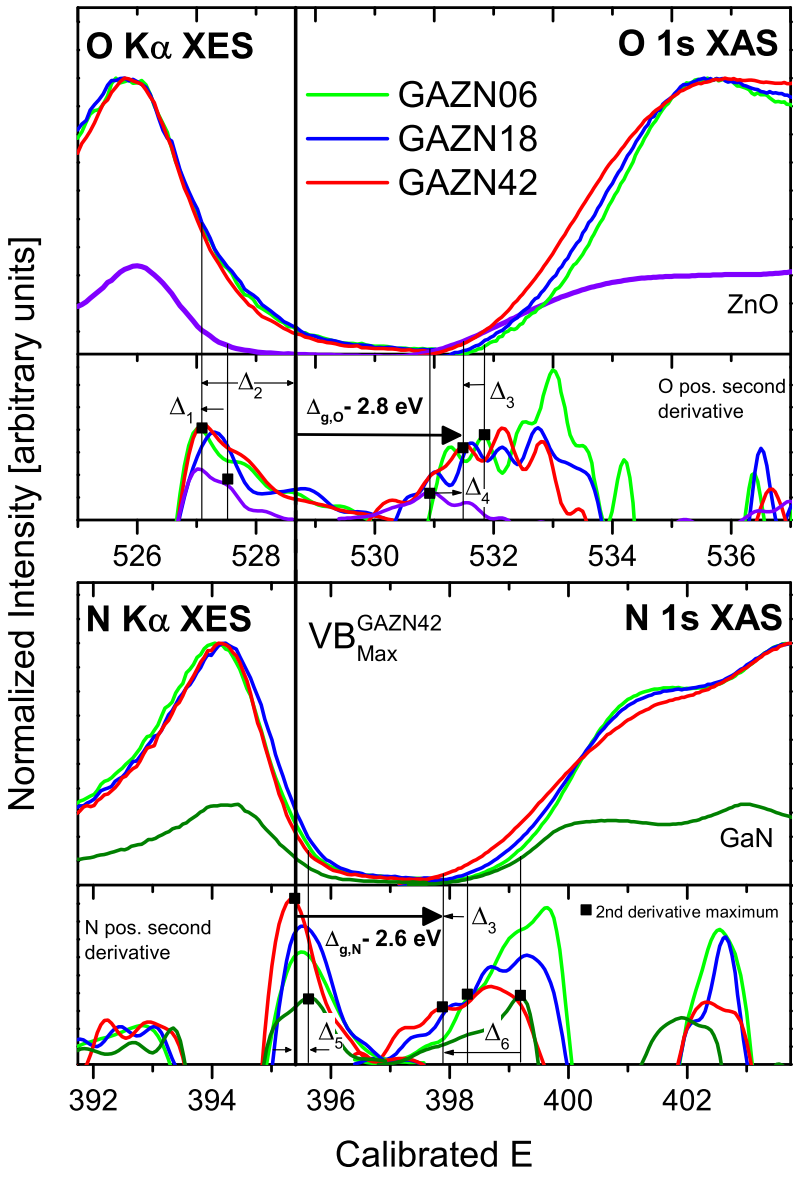

Figure 6.11: Band gap region of nitrogen and oxygen $K\alpha$ emission and absorption spectra of $(Ga_{1-x}Zn_x)(N_{1-x}O_x)$ for all samples, with positive second derivative of each spectrum plotted beneath. There is no significant shift in valence band onset between $x = 0.06$ and 0.42, but using second derivative of N *1s* XAS we measure a 0.4 eV reduction in band gap of GAZN42 (relative to GAZN06) in the conduction band onset energy. The displayed energy offsets are summarized in Table 6.3.

Table 6.3: Energy band offsets of sample GAZN42 as measured by second derivative of experimental spectra.

Offset	Energy offset ($\pm$0.1 eV)	Description
Δ_1	-0.4	Main O *2p* peak from ZnO to GAZN42
Δ_2	1.6	N *2p* - O *2p* onset difference for GAZN42
Δ_3	0.4	Band gap shift with concentration ($x = 0.06 \rightarrow 0.42$)
Δ_4	0.5	O CB edge shift from ZnO to GAZN42
Δ_5	-0.3	N VB edge shift from GaN to GAZN42
Δ_6	-1.1	N CB edge shift from GaN to GAZN42
$\Delta_{g,GaN}$	≈ 3.4	GaN VB to CB energy gap
$\Delta_{g,ZnO}$	≈ 3.4	ZnO VB to CB energy gap
$\Delta_{g,O}$	2.8	ZnO phase energy gap
$\Delta_{g,N}$	2.6	GaN phase energy gap

phase. This result is consistent with previously published UV-vis reflectance measurements of the GaN:ZnO system[7]. Using the experimentally determined offsets we can construct an energy diagram of the proposed dual-band gap heterojunction boundary, which is shown in 6.12.

The implications of a dual-band gap on a photocatalytic system are positive from an overall device standpoint. The existance of the 2.6 eV band gap allows a greater number of photons to be absorbed than pure ZnO, increasing the potential photocurrent for electrochemical reaction. However, if a 2.8 eV or higher energy photon is absorbed in the vicinity of the ZnO conduction band, the resulting excited state electron will lose less energy to thermal decay than if it had been excited to the GaN conduction band. This may allow the dual-gap solid solution to provide a slight additional overvoltage for H^+ reduction at surface ZnO sites, for example. Additionally, the heterojunction interface could assist in separating an exciton into independant holes and electrons. For example, a hole in the ZnO phase of the material would preferentially migrate to the GaN phase versus a conduction band electron. While a GaN valence band electron would give up 1.6 eV of free energy filling the ZnO hole, the ZnO electron would only lose 0.2 eV. Separation of excitons in this way would help alleviate carrier

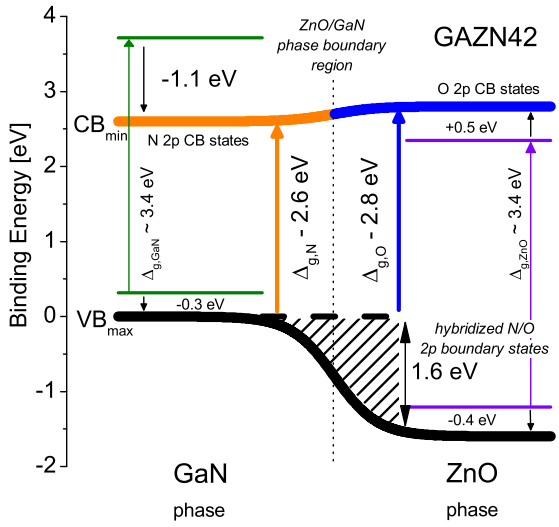

Figure 6.12: The proposed band transition scheme for $(Ga_{1-x}Zn_x)(N_{1-x}O_x)$ at $x = 0.42$, showing the two potential transitions in the GaN and ZnO components of the solid solution (2.6 and 2.8 eV, in agreement with UV-Vis measurements). The changes in band position from the precursor isolated GaN and ZnO to the solid solution phases are shown. Because of ZnO's dominance near the conduction band minimum the unoccupied band edges of GaN is repelled to lower energy, resulting in a reduced GaN band gap within an expanded ZnO gap.

recombination and hence the spontaneous loss of the energy absorbed from the photon that created that exciton.

6.6 Future work: GaInN:ZnO

A solid solution of GaN:ZnO with the addition of In has been reported to display improved photocatalytic activity over GaN:ZnO and displays enhanced absorption at lower energy visible light. We have studied GaInN:ZnO and GaIn:ZnO samples produced by the Maeda group with XAS and XES, and do see some evidence of a further decrease in the conduction band onset of N 2p states, as shown in Figure 6.13. Unfortunately, the samples we have studied that have undergone nitridation do not appear to be stable under intense X-ray excitation as the absorption spectrum shows a characteristic oscillation associated with N_2

gas absorption. While the absorption onset appears to be considerably reduced compared to the GAZN42 sample, it is unclear what portion of this might be the absorption edge of the N_2 gas or some damaged phase of the material that results from gas being released. There is also a slight shift upwards in energy of the valence band peak, though the second derivative does not shift up. This may imply that there exists a higher density of occupied states at the valence band without any actual band edge shift. This shift of the N *2p* states to higher energy is likely due to the inclusion of In 4s states in the valence band, which would have higher orbital energy than Ga 3s electrons.

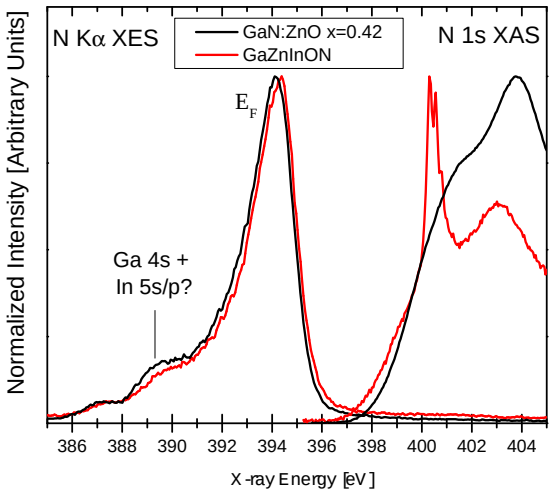

Figure 6.13: Comparison of GaInN:ZnO emission and absorption spectra to measurements of sample GAZN42. The key differences are a slight shift upwards in the valence band peak (though the XES second derivative peak occurs at the same energy), an enhancement of the Ga 4s feature in the XES possibly due to the contribution of In *5s* or *5p* states, and a substantial N_2 gas defect in the absorption spectrum centered at 400 eV. Note that the XAS peak at 404 eV in GAZN42 has shifted downward in energy along with the absorption onset energy; this may signify GaInN:ZnO has a lower band gap or that the inclusion of In in the material produces an enhanced core-hole effect in N absorption spectra.

Absorption results from GaInN:ZnO without the characteristic N_2 gas peaks have been published by Han *et al.*[82]. Their samples are prepared by a sol-gel method [83] which offers a high degree of crystallinity, which may explain their resistance to beam damage.

The absorption measurements are slightly broadened compared to GaN:ZnO, indicating that incorporating In could further shift the conduction band to lower energy. However, XES measurements of these samples are not available at this time, so it is premature to speculate on the degree to which the band gap could close. We are working in collaboration with this group to study their sol-gel samples, however at this time only XES measurements of their samples without In have been acquired. Future work is necessary to determine the effect of In on this system.

Chapter 7

Poly(triazine imide) Photocatalyst

7.1 Graphitic Carbon Nitride photocatalyst candidate

Polymerized carbon nitrides are one of the earliest discovered polymers, first reported by Berzelius and Liebig in the 1830's [84], but have been until recently been poorly understood because of their insolubility and the resulting difficulty in characterizing them. Interest in carbon nitrides intensified when a carbon nitride phase, β-C_3N_4, was predicted to be harder than diamond by Liu & Cohen[85]. It has been theorized that the beta phase could be synthesized from triazine or heptazine precursors (pictured in Figure 7.1), but the material was eventually synthesized using pulsed laser ablation [86]. In 2009, Wang reported H_2 evolution from a graphitic phase of carbon nitride in the presence of a sacrificial donor [6]. Wang's material was a form of melon, an old name given to polymeric tri-s-triazine, a graphitic phase with poorly understood interplanar stacking. Wang's observation was significant as the photocatalysis of water splitting had been previously limited to metallic compounds. Additionally, the material could theoretically behave as a heterogenous water splitter, as its valence band level was beneath the oxidation potential of O_2. Such a material, optimized and applied at industrial scale, could prove an inexpensive method of collecting and storing solar energy as hydrogen gas due to the outright abundance of carbon and nitrogen.

From a practical perspective, a carbon-nitride material has many qualities that would make it favourable for use in a solar-photocatalytic hydrogen production process. Graphitic carbon-nitride has been found to be stable over time while catalyzing water splitting reactions [6]; this durability would be important in producing reactors that operate continuously during daylight hours. Carbon and nitrogen are both abundant elements readily available for use in material manufacturing, ensuring large quantities of such a material could be produced

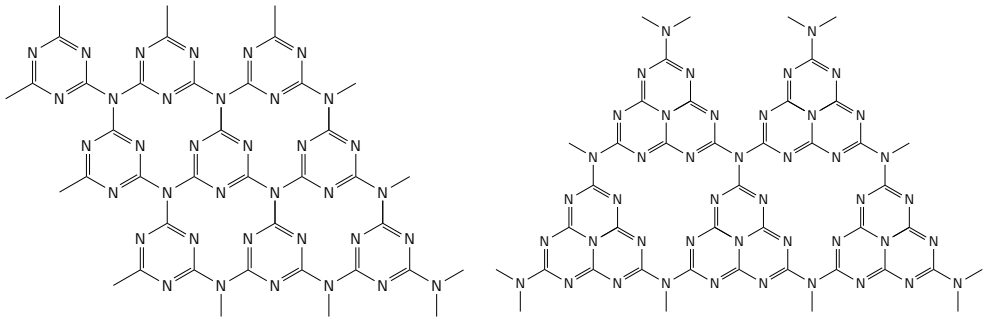

(a) imide-bridged triazine **(b)** imide-bridged heptazine

Figure 7.1: Comparison of imide-bridge triazine (a) versus heptazine (b). Two nitrogen sites occur in each structure: the N within the aromatic ring and the N in the amide bridge between rings. Note the central N in each heptazine ring that is not adjacent to free space within the layer. Adapted from Reference [6].

relatively inexpensively, especially compared to rare-earth catalysts. Additionally, for any proposed hydrogen generation or capture technology a significant amount of energy will be lost to store the hydrogen, which has poor energy density at standard temperature and pressure. Lowering the costs of all components of a hydrogen production process, including any novel materials required to enable the process, is important if it is to be an inexpensive input of energy into the economy.

7.2 Crystalline poly(triazine-imide) carbon-nitride material

Since 2010, we have been working with collaborators in the Schnick research group at Ludwig-Maximilians-Universität to investigate the electronic structure of a carbon nitride similar to the one discussed above: poly(triazine-imide), which will be referred to as PTI. PTI has a more densely linked graphitic structure than melon and has a regular stacking that causes pores to extend perpendicular to the graphitic plane through the structure. The pores of PTI provide coordination between the layers as they are filled with metalic salts which coordinate the carbon-nitride layers around them. Interestingly, the inclusion of Li and Cl in the PTI structure (PTI-LiCl) produces a dark brown powder that appears to absorb light at longer wavelengths than plain PTI or polymeric melon. PTI-LiCl also proves to be highly

crystalline, allowing its structure to be determined by XRD (shown in Figure 7.2 compared to the structure of melon).

The XRD structure of PTI-LiCl presents several challenges in its ability to be used to study the electronic structure of the material. First, the Li positions in the material can be found but only have an occupancy of 1/3, indicating only that they are all equally likely to be filled in the structure. Second, elemental analysis indicates that on average 2/3 of the Li sites should be occupied in the system, and the XRD structure leaves uncertainty as to structure the Li will exhibit [87]. Third, this published XRD structure gives no information about the location of hydrogen known to exist in the structure, but which is expected to be bound to the N sites that bridge adjacent C-N rings due to observed FTIR bands characteristic of C-NH-C units in melon and melam [87].

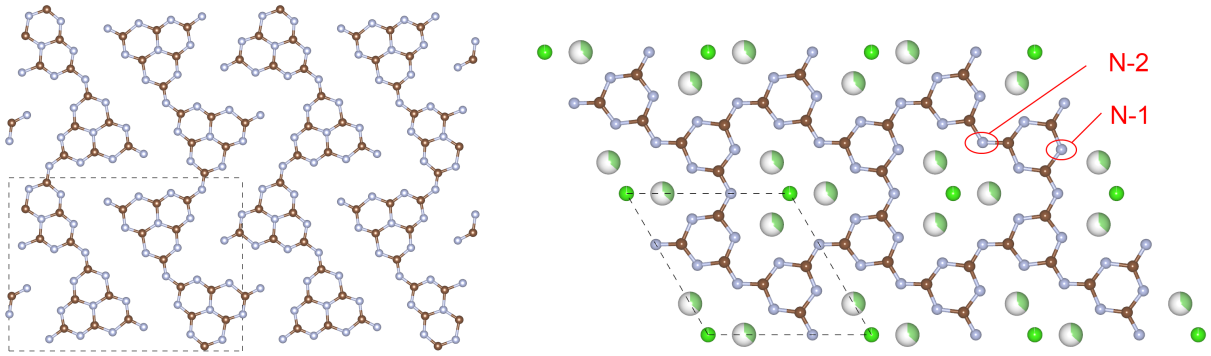

(a) Polymeric melon **(b)** PTI-LiCl XRD structure

Figure 7.2: Single layer XRD structures of melon and PTI-LiCl. Carbon is shown in brown, nitrogen blue, lithium in partially filled light green and chlorine in dark green. A single unit cell is shown with a dashed outline. The inequivalent N sites (N-1 and N-2) of PTI-LiCl are shown.

The PTI-LiCl samples were prepared by Eva Wirnhier by combining dicyandiamide (0.200 g, 2.38 mmol) with a eutectic mixture of lithium chloride (59.2 mol%, 0.904 g, 21.33 mmol) and potassium chloride (40.8 mol%, 1.096 g, 14.70 mmol) [87]. These precursors were ground together and transferred into a thick-walled silica glass tube. The tube was heated in a vertical furnace under argon atmosphere at a rate of 6 °C min^{-1} to 400 °C where they were held for 12 h. After heating, the samples were returned to room temperature at 6 °C min^{-1}. The tube was then evacuated and sealed with a hydrogen-oxygen burner at a length of 120 mm. The sealed tube was then heated to 600 °C at a rate of 10 K min^{-1} where it was held for 48 h.

The sealed tube was again returned to room temperature ($8\,\mathrm{K\,min^{-1}}$) and the contents washed twice with boiling water to remove any residual salt mixture. Finally, the PTI was dried at 200 °C under 5×10^{-4} mbar, resulting in 60 mg to 80 mg of dark brown powder. Elemental analysis of the resulting product showed molecular weights of C 29.6, H 1.3, N 50.4, Cl 11.0, Li 4.6, giving an expected molecular formula of $(C_3N_3)_2(NH_xLi_{1-x})_3 \cdot LiCl$ with $x \approx 0.33$ due to partial substitution of protons with Li^+ in the structure [87].

Because of the dark brown colour of PTI-LiCl as well as its structural similarity to polymeric melon it can be considered another candidate photocatalytic material. While PTI-LiCl itself has not yet been shown to catalyse water splitting, more amorphous formulations of the material demonstrate improved hydrogen production over melon under some conditions (Katharina Schwinghammer, private communication, June 20, 2012). The improved photoactivity of the PTI-like materials likely stem from the dark colour of PTI-LiCl, which indicates the material has a lower band gap than melon, and is therefore able to capture more of the solar spectrum as photocurrent. Investigation of this band gap has been challenging, as the material displays poor optical reflectivity for use in UV-Vis band gap measurements [Eva Wirnheir, personal communication, May 23, 2012].

Due to the challenge in characterizing the band gap of PTI-LiCl, we have performed XANES and XES measurements of powdered samples of the material to attempt to quantify the band gap of the material. An investigation of the electronic structure, particularly by XES, has also been able to provide insight into the mechanism for band gap reduction of PTI versus melon as well as to resolve some of the challenges in determining the structure of PTI-LiCl mentioned above.

7.3 Soft X-ray measurements of PTI-LiCl

To characterize the band gap of PTI-LiCl, it was necessary to measure both the valence and conduction band using soft X-ray techniques. Since PTI is a covalently bonded material, we should be able to then determine a band gap by comparing the band onset energies of either the C or N measurements of the material. As both C and N will contribute *2p* states to the valence and conduction bands the choice of which element to use should be arbitrary.

However, N *2p* electrons have higher orbital energy than C *2p* states and should occupy the upper levels of the valence band, providing a more direct probe of the valence band maximum. Additionally, N *2p* XES measurements typically exhibit a very sharp onset at high energy; this is ideal for our method of using the second derivative to choose the valence band onset position as the sharp onset will create a sharp derivative peak.

However, the choice of N spectra complicates the problem of band gap measurement: there are two inequivalent N sites in the system (which shall be labelled N-1 and N-2). N1 is a member of the triazine ring, where it is bonded with two carbons only. N-2 links two triazine rings by bonding again with two carbons, however it also has a free bond directed into the pore of the PTI layer that can bond with either H or Li. The importance of the inequivalent N sites will be discussed in further detail below, however it is important to note that each site can contribute distinct electronic states within the conduction and valence bands that must be accounted for when determining a band gap.

Using the N absorption edge, a band gap determination of 2.2 eV can be made as illustrated in Figure 7.3. This band is predicated on a core-hole shift of 0.43 eV determined by a DFT core-hole model which will be discussed below. The XES measurement is performed non-resonantly ($E_{excitation} = 420\,\text{eV}$) in order to ensure neither inequivalent N site is preferentially excited. Evidence of the inequivalent N sites is present in the splitting of the XES peak, and two features in the absorption band have been labelled to indicate which inequivalent N site dominates the density of states at this energy (this will be further discussed below).

Carbon measurements of PTI-LiCl could also be used to characterize the band gap, however the carbon XES measurements are less tractable due to their inclusion of N *2p* hybridization features at the upper energy of the band, as well as their relatively higher degree of noise. Additionally, C absorption suffers from a relatively large core-hole shift that pulls the π^* band into the conduction band, giving the material the (inaccurate) appearance of a metal. Carbon spectra are presented in Figure 7.4 for reference. There is again evidence of the presence of inequivalent N sites as can be seen by the splitting of the π^* feature at 288 eV.

Of concern when using the N spectra for band gap determination is the exact nature of the contribution to the emission spectra by inequivalent sites. If the N *2p* DOS is sufficiently localized to each site, it might be possible that the valence and conduction band edges do not

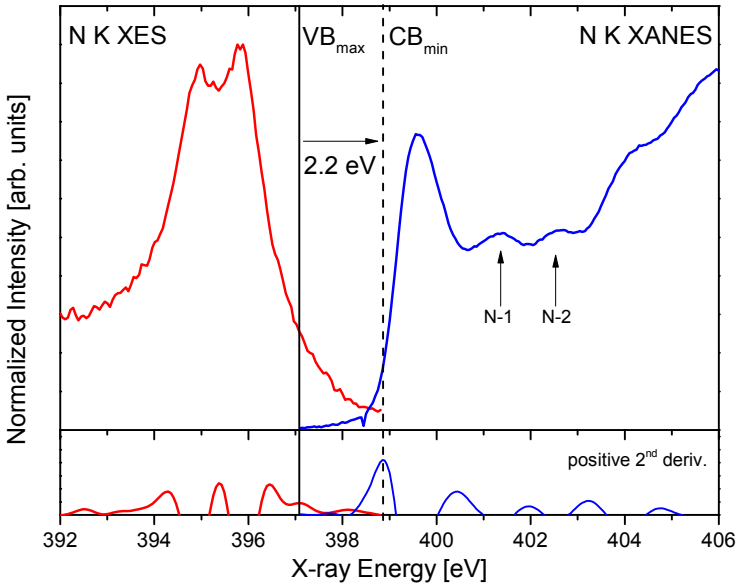

Figure 7.3: Facile band gap determination of PTI-LiCl using N *2p* states (Kα XES and *1s* XANES). A core-hole effect of 0.43 eV is determined using the DFT model discussed below and added to the measured XES-XAS gap.

correspond to states on the same N site, making the minimum transition energy impossible if there was too little orbital overlap between sites. To investigate this effect, a series of resonant XES spectra were conducted to attempt to discern the contribution of each site. When taking an XES measurement, the core hole that is produced is created by an incoming X-ray. By sweeping the incoming X-ray energy through the conduction band projection of the atom of interest it is possible to selectively excite into particular conduction band states. However, if particular conduction band states are associated with a particular atomic site's core state then those core states will be preferentially vacated. The resulting valence to core transition measured in the emission spectrum will therefore be resonantly enhanced, resulting in an emission spectrum with features characteristic of the electronic structure of that atomic site.

Emission spectra of PTI-LiCl were collected as the exciting X-ray energy was swept across the N conduction band in 0.5 eV steps. Selected spectra that show resonant features are presented in Figure 7.5 along with the absorption spectrum features they correspond to. The measurements confirm the above prediction that inequivalent N sites are contributing states to the band edges: N-2 contributes the states at the valence band maximum while N-1 contributes the conduction band minimum states. At this point in the analysis, it can

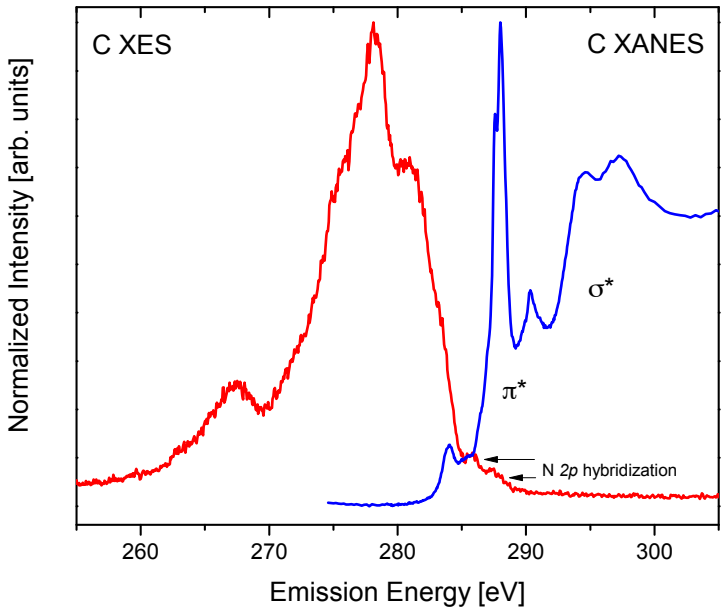

Figure 7.4: C XES and XANES of PTI-LiCl. Neither measurement was well suited for band gap determination due to the high degree of noise in the emission spectrum and the significant core-hole shifting in the absorption spectrum.

no longer be taken as a given that the band gap measured in Figure 7.3 is correct without knowing more about how the N-1 and N-2 sites interact. In order to say more about the band gap of this PTI-LiCl it is necessary to have a theoretical model to interpret the experimental results.

7.4 DFT modelling of PTI-LiCl

As discussed above, a model of the electronic structure of PTI-LiCl is necessary to interpret the measured spectra of the system. As with any other X-ray band gap determinations made, an estimate of the core-hole induced shift downward in energy that occurs in the absorption measurement is necessary in order for the gap to be credible. Additionally, in the case of PTI-LiCl it becomes necessary to determine the contribution of inequivalent N sites to the conduction and valence band edges. Unfortunately, there remained the challenge of defining a structural model of PTI-LiCl given the incomplete information provided by the previous XRD and NMR measurements [87]. However, enough structural information was available to approach the problem using an iterative approach to solving the unknowns.

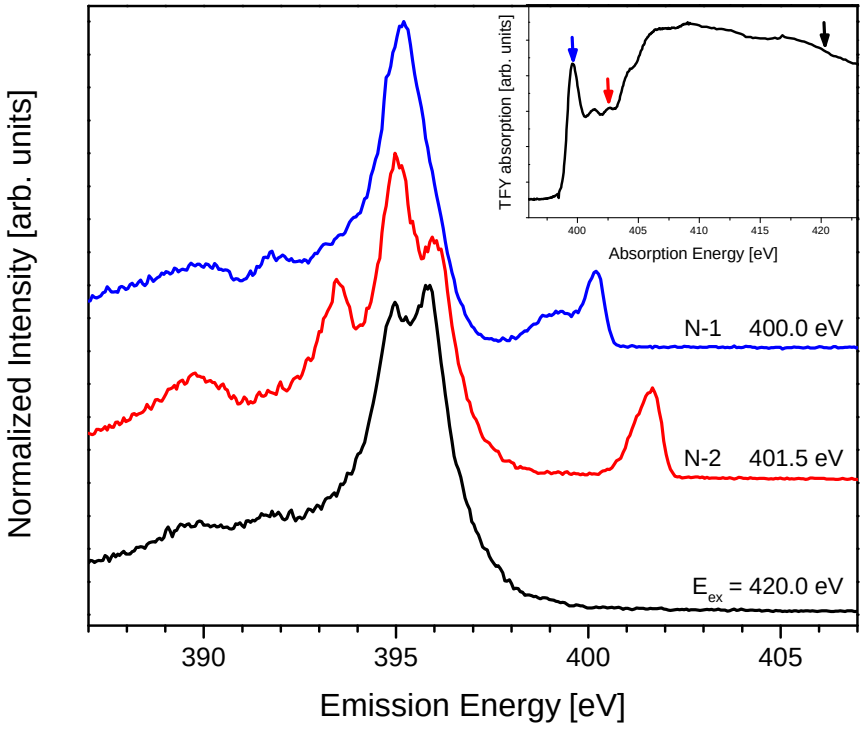

Figure 7.5: Resonantly excited XES of the PTI-LiCl N-1 site (blue), N-2 site (red) as compared to the non-resonant spectrum (black). The inset shows the features in the N absorption spectrum that were excited using arrows of the same colour. Selective excitation of the the N-2 site shows that it contributes most strongly to the feature at the valence band maximum. Both resonant excitations show improvement in different C-N hybridization features below the main peak (at 391.7 and 393.5 eV).

In order to produce a workable structural model, WIEN2k was used to perform DFT calculations and force optimizations of a series of structural candidates. Upon converging an electronic structure solution for each candidate the observable calculated results could be compared to our experimental data to determine model quality. Several quality tests were available to use. The primary test was the calculated band gap of the material, which should be less than the measured band gap (as DFT typically underestimates the band gap in most systems [25]). Additionally, the partial density of states and calculated X-ray spectra produced by the model should be comparable to the features to the experimental spectra. Finally, the model structure should maintain the symmetry of the original XRD structure after force relaxation.

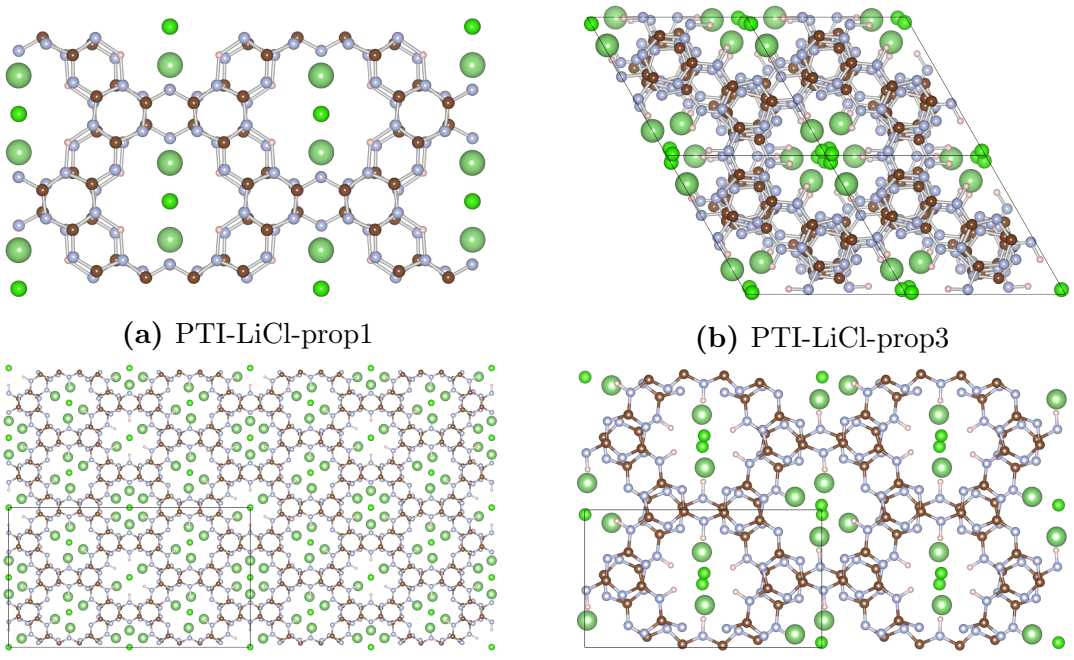

(a) PTI-LiCl-prop1

(b) PTI-LiCl-prop3

(c) PTI-LiCl-prop10

(d) PTI-LiCl-prop13

Figure 7.6: Example structural candidates used for DFT calculations. PTI-LiCl-prop13 was finally found to have enough features in common with experiment to use as a model for PTI-LiCl. All structures observe the same AB layer stacking as the PTI-LiCl XRD structure in Figure 7.2.

Initially, structural models were attempted with the assumption that Li and H substitute for each other in the unit cell due to their similar proclivity to ionize when in a solid system. An initial structure shown in Figure 7.6a (PTI-LiCl-prop1) was force optimized, producing electronic structures with reasonable band gaps. However, this structure forces the bonding of the C-N layer to be fully conjugate as each N site has only two nearest C neighbours. This bonding arrangement is not compatible with the system having two inequivalent N sites and does not correctly reproduce the valence or conduction band features of the measurement as a result. Additionally, this structure only remained stable under force optimization when the original symmetry of the system is enforced (i.e. the structure is expressed in terms of the $P6_3cm$ space group).

After the initial structures failed the next calculations were made removing the symmetry restriction, however this immediately resulted in unstable structures under force optimization. The next step was to introduce Li disorder into the system by producing a $1 \times 1 \times 3$ supercell of the original XRD structure and rotating pairs of Li along the c axis, as shown in Figure

7.6b (PTI-LiCl-prop3). This was done with the goal of cancelling the dipole moment in the a-b plane by eliminating the preferred polarization direction introduced by the Li-Cl pair, which would be expected to exchange an electron in the solid due to the relative difference in electronegativity between the two elements. At this point it was also decided that the C-N ring-linking N-2 site must not be conjugately bonded, but should instead be bonded to an H in plane with the C-N layer, producing a C-NH-C group facing into the pores of the PTI system. To model this, 3 hydrogen atoms were introduced per unit cell of the original XRD structure and the N-H bond length force optimized. However, several attempts to optimize the forces of this new structure proved unstable as well, and the Li disordering did not sufficiently reproduce the features of the N *1s* absorption spectrum.

An additional factor worth noting at this point is that all structures attempted so far that did not have their symmetry enforced during force-relaxation would tend to lose the corrugated structure of the C-N layer, which would instead flatten into a single plane. There was some experimental evidence in the XRD measurements that in PTI-LiCl samples with reduced Li content the interlayer stacking distance would increase slightly, an effect that could be attributed to a flattening of the C-N layers. This suggested that up to this point the amount of Li in the DFT models was too low.

Finally, it was hypothesized that Li substituting for H could resolve the decreased band gap issue with the previous set of structural candidates. It had been noted in previous calculations that Cl *2p* states were the predominant component of the total density of states at the valence band maximum. Since Li is expected to lose its *2s* electron to the Cl *2p* shell, the inclusion of more Li in the system should contribute more states to the top of the valence band, perhaps closing the band gap. Additionally, there was evidence from solid state NMR measurements of PTI-LiCl that Li-H substitution was occurring, and that amount of Li included in the earlier models was insufficient to match the elemental composition of the PTI-LiCl product (although this assumed that all precursor Li had been removed from the samples) [87]. To investigate this possibility, several structural candidates were optimized that contained two or three Li per pore and force optimized. For example, PTI-LiCl-prop10 (Fig. 7.6c) contained pores with 1, 2 and 3 Li. As an H per pore had each new Li, several more symmetry types were possible. Several candidates were rejected because upon force relaxation the Li would

occupy opposite positions around the Cl position in the same plane; this broke the threefold symmetry of the original XRD structure and had to be rejected. However, one structure was stable, with two Li per pore stabilized by two H opposite to them as shown in Figure 7.6d. The Li positions in this structure did obey the 3 fold symmetry of the original XRD structure and the H were able to maintain this by repulsion.

Now that an appropriate model for the positions of 4 H and 2 Li in a C-N pore was established, it remained necessary to approximate the correct degree of deprotonation. The ratio of H to Li in the elemental analysis indicates about at 2:1 ratio, however structural candidates in which every pore had 4 H and 2 Li proved to be unstable under force optimization. Instead a model in which half of the pores had 2 Li and the other half had 1 Li was attempted, (a 5:3 ratio). This model (labelled PTI-LiCl-prop13), shown in Figure 7.6d, proved to pass all the fitness tests listed above. It had a calculated band gap of approximately 2.4 eV, slightly higher than desired but this was expected given the intentionally low loading of Li. Additionally the symmetry was correct.

Calculated X-ray spectra from the PTI-LiCl-prop13 model agree well with the measured spectra, as shown in Figure 7.7. Breaking down the total calculated N *1s* X-ray absorption spectra by site, this structure reproduces the splitting observed in the resonant emission experiment. The agreement extends to the valence band as well. In Figure 7.8 we have used the calculated model to align the C and N Kα XES measurements on the C emission energy scale. As N *2p* states occupy the upper energies of the valence band, they are able to hybridize with the upper C *2p* states as can be observed at the high energy end of the C emission spectrum. Indeed the splitting between the two inequivalent N sites is visible in the C measurement, indicating that hybridization is occurring on all C sites (as would be expected if the C atoms retain an equivalent bonding environment). The resonant features in the N-2 emission measurement also show good agreement with the calculated spectrum and their contribution to the C-N *2p* mixing in the centre of the valence band becomes apparent as well.

With a suitable DFT model of the PTI-LiCl available it was possible to find the conduction band onset shift due to the presence of a core hole, which was found to be 0.43 eV as mentioned above. It was now possible to use this value to extract a band gap from the XES and XAS

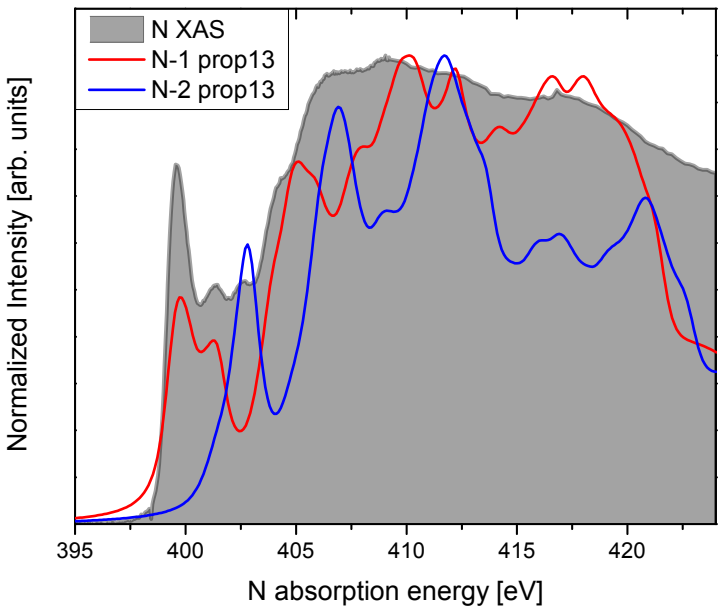

Figure 7.7: Calculated X-ray absorption spectra of the inequivalent N sites (N-1 in red, N-2 in blue) as compared to the experimental N *1s* XANES spectrum (shaded). The calculation is able to produce the low energy features that split between the two N sites particularly well. The normalized intensity of each calculated spectrum reflects only the contribution of a single atomic site.

spectra as presented in Figure 7.3. This band gap value is in agreement with currently unpublished measurements taken using UV-Vis reflectance (a low quality measurement showing approximately 2.6 eV) and monochromated EELS (2.2 eV) [Prof. Christina Scheu, private presentation, June 20, 2012].

7.5 PTI band gap versus Li loading

Now that a suitable estimate of the PTI-LiCl band gap was available it was of interest to explain the mechanism by which its decrease occurred as compared to melon. This was facilitated by measurements of PTI samples with reduced LiCl content. Samples with approximately half and one quarter the LiCl content of PTI-LiCl as well as with a negligible amount of LiCl were produced by extracting the intercalated slat using a soxhlet extraction (performed by our collaborators). The resulting samples when dried displayed a lighter, yellower colour, suggesting that they may have a higher band gap.

As show in Figure 7.9 XES measurements of the PTI samples with reduced LiCl do in

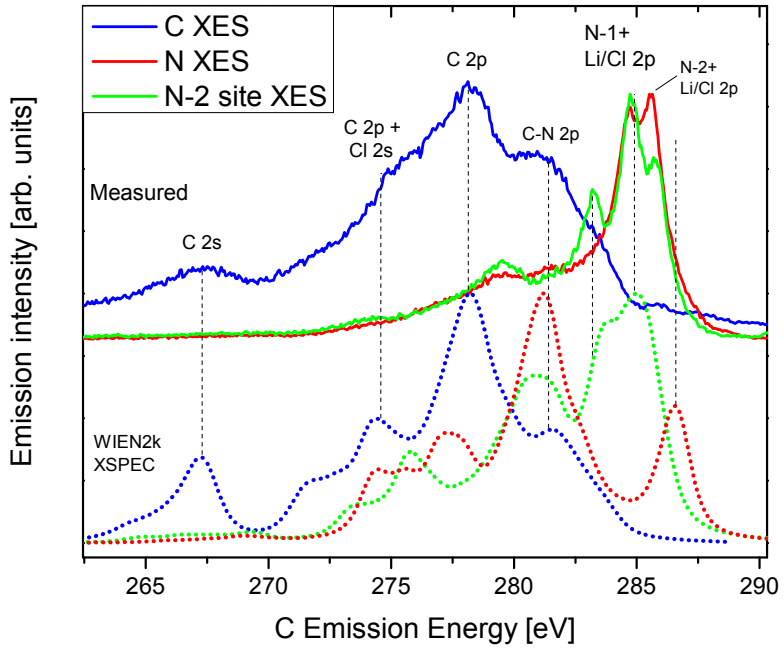

Figure 7.8: Comparison of the XES measurements with calculated emission spectra from PTI-LiCl-prop13. The calculated C emission spectrum reproduces the experiment very well with all major features accounted for, including an appropriate amount of splitting between the C *2p* valence states and the lower energy C *2p*/*2s* sub-band. The N Kα emission alignment with the C energy scale also shows agreement with the calculated features of the N-2 emission spectrum.

fact show an increased band gap due to an apparent downward shift of the valence band maximum. The reduced LiCl samples also have a more gradual conduction band onset than PTI-LiCl, however the point of onset as determined by a second derivative remains constant. Both the emission and absorption measurements begin to lose the features that proved linked to the inequivalent bonding environment of the N sites in the analysis above, which intuitively makes sense if the sample is losing N-Li pairs. With the absence of Li states in the valence band, the split N peak in PTI-LiCl relaxes into a single, broader feature with an energy onset approximately 0.7 eV lower than PTI-LiCl.

It is therefore apparent that loading the PTI structure with LiCl to the point of creating N-Li pairs is necessary to achieve the low band gap of PTI-LiCl. Without sufficient Li content to displacing H from N-H bonds in the pores, there simply will not be enough Li

state hybridization at the top of the valence band to induce the observed splitting effect. It could also be argued that the order of operations in synthesizing the material is important: if PTI-$(LiCl)_{0.5}$ could be produced by introducing LiCl to an already formed C-N matrix one would expect the Li to not substitute into existing N-H bonds, but instead since Li is being removed (at random) from an already fully loaded PTI sample, some N-Li bonds should still exist, giving the small degree of peak splitting observed in the measurement.

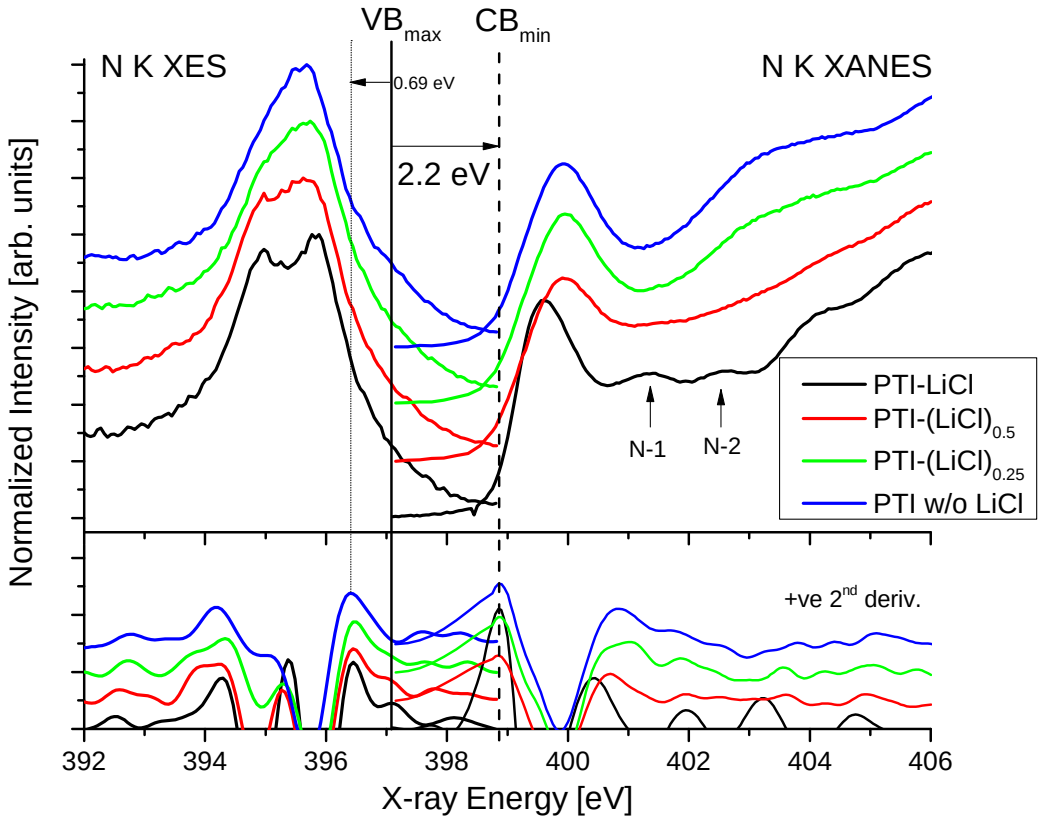

Figure 7.9: Comparison of band gap plots for PTI-LiCl as well as PTI with one half, one quarter and negligible LiCl content. As Li is removed from the sample the features characteristic of N site splitting diminish and are finally quenched. This appears to be coupled with a relaxation of states away from the band gap coupled with a decrease of the valence band maximum by $\approx 0.7\,\text{eV}$ from PTI-LiCl to bare PTI.

7.6 Future work

The above analysis of PTI measurements and calculations is being compiled into a manuscript that will hopefully be in draft form by September 2012. There remains some further work on simulating the removal of Cl from the structure as well as analyzing the contribution of Cl *2p* states to the valence band. Cl *2p* states provide a substantial contribution to the total DOS of the valence band maximum, however the isolation of Cl within the structure calls into question the localization of these states. If it can be shown that these states hybridize with N *2p* states then a more convincing case for the band gap measurement in PTI-LiCl, especially since the calculated model in Figure 7.8 shows an N-1 site feature at the top of the valence band that is not observed during the resonant N-1 XES measurement. This feature could be related to N-Cl state hybridization, and its absence in the resonant emission scan could be explained by a lack of Cl states at the bottom of the conduction band.

Additionally, as discussed in Chapter 5 there is a considerable gap between understanding of the homogeneous band structure of a photocatalyst and its electronic structure at the surface. Further study of the surface of PTI-LiCl seems key to explaining its apparent lack of photocatalytic activity compared to melon or more amorphous PTI compounds. The creation of appropriate surface models of the PTI C-N matrix seems relevant, as well as the ability to simulate the adsorption of waterborne species (OH^-, H_3O^+) would be very useful in the theoretical study of PTI as well as other photocatalytic systems.

Also, we have measured additional PTI samples that contain Br, Zn, Cu, Fe and P as a result of intercalation. These samples have shown poor crystallinity in XRD measurements and so their theoretical study will require more careful modelling and force-optimization of structures. Though none of these materials present as low a band gap as PTI-LiCl it would still be useful in understanding the limits of photocatalytic carbon nitride systems to promote photocatalysis, and further study is warranted.

Chapter 8

Surface versus bulk characterization of Li K-edge in Lithium Compounds

8.1 Introduction

Modern developments in lithium batteries that incorporate alloying electrochemistry are highly dependant on the use of electrodes incorporating Li ions [17]. At the surface of such a battery electrode that relies on redox processes to retain lithium, it is possible for various unwanted organic and inorganic side products to form. During routine cycling these organic compounds can impact battery performance, either by enabling detrimental side reactions to occur or simply by building up over time to passivate the electrode. Little is known about the nature of these side reactions, as the products do not form in large quantities suitable for characterization by conventional chemical techniques.

There is also little available X-ray spectroscopic data on organic lithium species. While LiOH absorption was first reported in 1937 [88] by means of ruled spectrographs and spark bulbs, few high resolution synchrotron based spectra have been published. Tsuji *et al.* reported TEY spectra of several lithium oxides measured on the compact synchrotron facility at Rtsumeikan University, however the spectra were quite noisy [89]. A good literature review of other Li K-edge absorption spectra has been compiled by Braun *et al.* who notes the sparse number of published spectra [90]. Since most synchrotron facilities are designed with high energy X-ray experiments in mind, there are a limited number of beamlines designed specifically to measure absorption in the region of the Li K-edge. However, the VLS PGM beamline at the CLS is an exception, providing X-rays down to an energy of 5.5 eV generated by a planar undulator insertion device, making it a good candidate facility to expand the

published dataset of Li absorption spectra.

The study of Li species is hampered by a number of factors, including its low atomic weight, low electronegativity and its sensitivity to its environment [91]. On the surface of an electrode there can be many undesirable chemical species in addition to the phase of interest in which Li ions are stored. High chemical sensitivity is necessary to discriminate between the two forms of Li, particularly if side-products constitute a minority of the Li present. This work compares various methods of synchrotron X-ray probes to discriminate between prepared lithium organic samples in order to establish the necessary data set with which to analyze the Li content of actual electrodes. We compare two methods of measuring XANES (TEY and TFY) with measurements acquired by X-ray Raman Scattering (XRS). Soft X-ray XANES probes the surface region of our samples, while a transmitting hard X-ray is used in XRS to probes the bulk of each sample. XANES and XRS both achieve chemical sensitivity by probing the unoccupied states accessible to a Li *1s* electron, which are influenced by the local environment such as bond length, site symmetry and bonded element. The different measurement techniques can therefore be used to build a picture of the chemical composition and electronic structure of the surface of lithium compounds in contrast to the bulk. This work may then be extended in the future to examine the Li organics present on an actual electrode sample.

In the present work we have improved on the signal-to-noise ratio of several published measurements [89, 90], as well as investigated the effect of X-ray beam damage on the sub-surface of the sample by XANES. Li organic powders and alloyed electrode samples have been prepared for us by Ulrike Boesenberg and other collaborators at the Lawrence Berkeley National Laboratory (LBNL) for our measurements. We plan to combine our experimental study with DFT calculations performed with both all-electron (WIEN2k) and pseudopotential plus plane-wave (Quantum Espresso) basis sets performed by our LBNL collaborators to model the Li conduction band. In addition to our Li XAS spectra, Li K-edge XRS measurements have been collected by our collaborators at Stanford, who have in the past modelled their measurements by using Bethe-Salpeter equation (BSE) calculations to simulate the excited state transition [92, 93].

8.2 Experimental Measurements

The Li 1s XANES measurements were performed at the variable line spacing plane grating monochromator (VLS PGM) beamline at the Canadian Light Source. Spectra were measured simultaneously in both total electron yield (TEY) and total fluorescence yield (TFY) and normalized to the incident beam current as measured by a transparent nickel mesh upstream from the sample. All samples were measured with the surface normal parallel to the incident radiation. TEY data was collected with a nanoammeter connected to the sample ground, while TFY data was recorded using a channel plate fluorescence detector mounted 45 degrees relative to the incident beam. Samples were mounted on indium foil scraped of surface oxide under non-reactive atmosphere, then transferred to ultrahigh vacuum (5 x 10-7 torr or better) for measurement.

Figure 8.2 displays a comparison of XRS and TFY measurements for the measured samples. Good agreement is achieved in the more stable samples (LiF, Li_2CO_3, Li_2SO_4) while the more sensitive samples show significant disagreement between the edge onset and features. This can be attributed to several factors, including surface contamination and oxidation of the samples or beam damage from the intense, on-resonant synchrotron light probe, which affect the XANES measurements. Because the XRS measurements are made in transmission, the interaction volume of the measurement is significantly higher, reducing the influence of any surface contamination or beam damage. The impact of beam damage is of greater significance in the XANES TFY measurement of Li, as the beam interaction volume is particularly small on account of the low beam attenuation length at the Li K-edge (between 20 nm to 50 nm [41]). Also it is expected that an Li^+ ion subject to a core hole excitation would be particularly reactive given its poorly screened nuclear charge.

8.3 DFT Calculations

All electron DFT calculations of the Li K-edge were performed for the mesured samples using the WIEN2K code [26]. The generalized gradient approximation (GGA) was used as the DFT functional. The excited Li state was modelled by building a $2 \times 2 \times 2$ supercell from

published crystal structures [77] and introducing a core-level vacancy. Charge balance was maintained by applying a background charge of 1 e^-. The pseudo-ground state was then solved self consistently and the resulting solution used with the XSPEC code to calculate the XANES spectrum within a spherical region around the excited lithium. However, the pseudo-ground state was found to over-estimate the core-hole effect, as shown in Figure 8.1 for the calculated DOS of LiF. This is unsurprising, as the Li site modelled in this way is particularly non-physical: a nucleus with a charge or +3 is being screened by a single *1s* electron, pulling the valence and conduction band states down in energy. To properly model the excited state, the X-ray excited electron should be placed in a conduction band state localized to the Li site (as an exciton), however this is not a ground-state effect that can be modelled directly with DFT. BSE [92] can be used to model this exciton but these calculations are particularly expensive. Further calculations are being performed by our collaborators to compare with the experimental spectrum in an effort to better model the electronic structure of Li during a core-level excitation.

8.4 Analysis of Experimental Results

As the surface chemistry of lithium compounds is of practical interest as discussed above, it is instructive to compare the most surface-sensitive measurements to bulk measurements. The bulk electronic structure of a material system can be thoroughly understood through the calculation methods mentioned above, but the aperiodicity of a material's surface becomes difficult to model and simplifying assumptions must be made. However, experiments make it possible to probe different regions of each sample in order to compare their electronic structure.

Due to the extremely low X-ray energies used for these XANES measurements, the attenuation length of the exciting beam is expected to change significantly over the energy range scanned. In addition, the Li K edge energy (54.5 eV) is very close to the O L_1 edge (41.6 eV), and many of the measured samples contain oxygen either intrinsically or through contamination. As a result, 4th or 5th order polynomial background were fitted to the energy region outside the Li edge and subtracted.

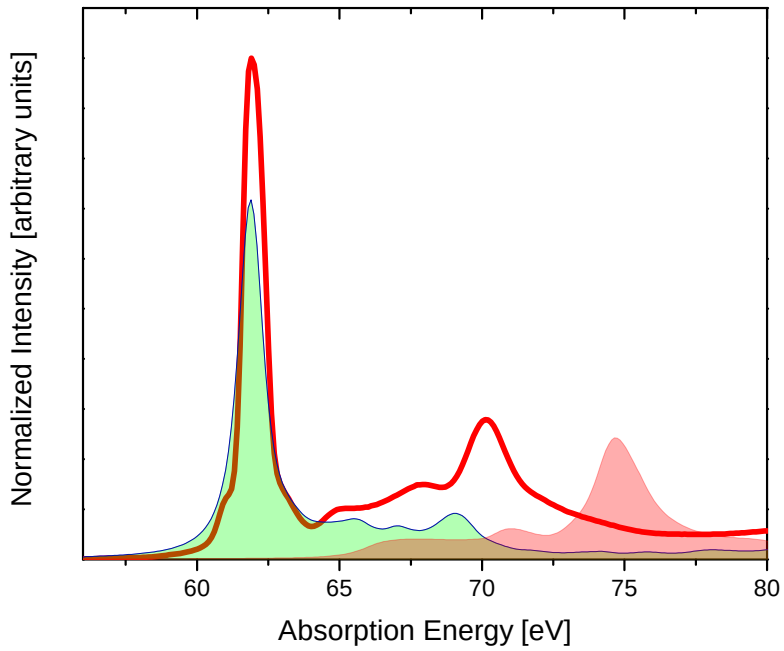

Figure 8.1: Lithium absorption (red line) versus calculated X-ray absorption for LiF, using both a normal unit cell (red fill) and a $2 \times 2 \times 2$ supercell structure with a core-hole included (green fill). While the core hole calculation does a good job of reproducing exciton features of the absorption spectrum, the core-hole causes significant downward shifting of the conduction band absorption states, and does not well reproduce the measurement. The overcompensation of this shift with respect to the exciton position suggests that the complete core-hole effect is over-emphasized in this calculation.

The comparison of Li_3N spectra in Figure 8.2a shows the least agreement of all spectra presented, due to what appears to be a $LiNO_3$ contaminant in the X-ray measurement. In the TFY spectrum, the Li_3N conduction band onset at approximately 55 eV is evident, however the remainder of the spectral features appear to better match the $LiNO_3$ spectra (solid red line) with features repelled higher and lower in energy by the presence of the states described by the XRS peak at 60.8 eV. This effect is not as pronounced in the lower-energy peak of the TEY spectrum, suggesting that contamination could arise in the sample sub-surface by beam damage. The X-ray spectra are also quite distinct from Li_2O (Fig. 8.2b), indicating that total oxidation of the lithium sites is not occurring; again this suggests beam damage rather than environmental oxidation.

LiF (Fig 8.2c) is well reproduced under all three measurement techniques, with the XRS

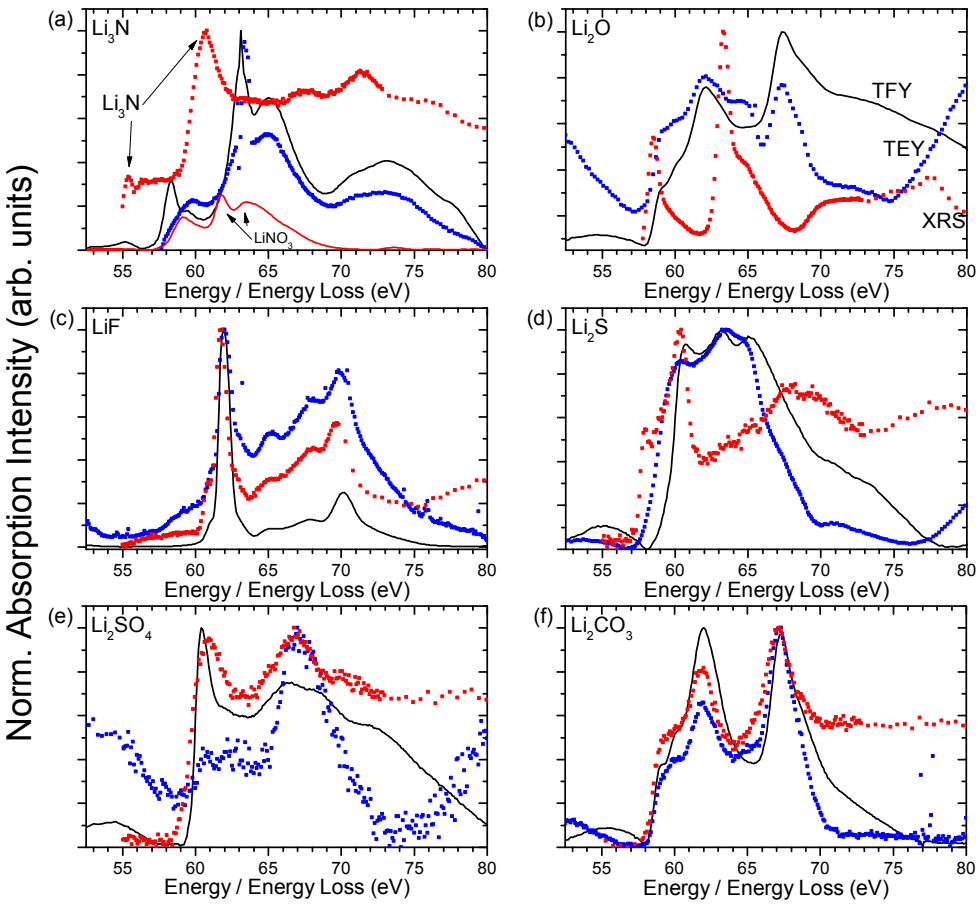

Figure 8.2: Lithium K-edge spectra of the organic lithium compounds studied. XANES TFY (black), TEY (blue) and XRS (red) are displayed.

measurement giving a good indication of the self-absorption orrucing in the TFY measurement The TFY spectrum of Li_2S (Fig 8.2d) also suggests significant oxidation is occurring in the bulk of the measured sample. It should be noted that the TEY onset is in much better agreement with the XRS measurement than TFY, suggesting that oxidation damage is occurring beneath the surface during the TFY measurement. The XRS measurement also displays a sharp pre-edge feature that has been broadened out in the TFY, indicating that some damage is still likely occurring on the surface.

Li_2SO_4 and Li_2CO_3 (Fig 8.2e and 8.2f) show good agreement between all three measurement techniques, however the high band gap of Li_2SO_4 gives it poor surface conductivity, reducing the quality of the TEY measurement. In Li_2SO_4, the differences in peak intensity between TFY and XRS indicate that the higher energy peak around 67 eV suffers from self-absorption.

It is interesting to note that this feature is dominant in the TEY spectrum, suggesting that these are weakly bound continuum states.

8.5 Future Work

Upon cursory analysis, XANES TEY measurements of lithium compounds are comparable to XRS bulk measurements, indicating the bulk crystal structure is reasonably conserved on the surface of these powders. If Li species surface structure can be shown to be preserved in a more thorough way, XANES TEY may be a useful technique in studying electrode surfaces, perhaps using a principal component analysis technique. As Li absorption measurements have already been taken of electrode samples provided by our collaborators, further analysis should be performed in the future.

A manuscript describing these measurements is currently in circulation with our collaborators, who are expected to add their calculated results by the end of August 2012. Once these results are available, further interpretation of the measurements may be possible.

Chapter 9

Conclusions

9.1 GaN:ZnO photocatalyst

The lack of observed O-N 2p hybridization occurring near the valence band maximum allow our measurements of GaN:ZnO samples to be best described as a solid solution heterostructure of GaN and ZnO phases, both of which display similar electronic structure to precursor materials. Measurements and calculations of the electronic structure of the GaN:ZnO solid solution, including observations of N *2p*-Zn *3d* and O *2p*-Ga *3d* hybridization on phase boundaries, were used to align spectra into a binding energy picture in order to understand the valence band and conduction band composition of the material

The band gap decrease of GaN:ZnO over either precursor material have been shown to occur due to a decrease in the minimum energy of the conduction band onset, contrary to some earlier reports which suggested the band gap should be reduced by an increase in the valence band maximum. The mechanism for this decrease is attributed to a repulsion of unoccupied N *2p* states moving to lower energy by the introduction of unoccupied O *2p* states at higher energy. Because N *2p* states also compose the valence band maximum, the result is an inverted heterojunction band gap.

By using the second derivative of our measured spectra we have estimated two optical band gaps for $(Ga_{1-x}Zn_x)(N_{1-x}O_x)$ at $x = 0.42$: 2.6 eV arising from valence band maximum transitions to the GaN phase conduction band and 2.8 eV transitions to the ZnO phase conduction band. This result is in qualitative agreement with previous UV-Vis measurements and studies demonstrating the existence of multiple optical transitions in the material.

9.2 PTI-LiCl

A structural model of the PTI-LiCl photocatalyst candidate is presented and compared to X-ray emission and absorption spectra, after having achieved fitness in three calculated metrics: band gap, reproduction of spectral features and overall crystal symmetry. This structural model has been used to calculate the electronic properties of PTI-LiCl, producing results that are in good agreement with experimental measurements.

This PTI model allows us to understand the band gap decrease of PTI-LiCl in terms of its Li loading. Increased Li loading leads to an injection of Li states at the valence band maximum due to Li *2p* state hybridization with the N-2 site in the structure. This hybridization causes splitting of the N Kα emission peak, forcing some N *2p* states to higher orbital energy. This repulsive effect closes the band gap from the valence band side by 0.7 eV versus a sample without Li loading.

9.3 Li materials

Several Li XANES measurements of Li organic powders are presented in comparison to XRS measurements of the same compounds, showing good agreement in most instances. DFT calculations on the Li compounds have been attempted using WIEN2k, however they are in poor agreement with the experimental results due to the exaggerated effect of a static *1s* core-hole on an ionized Li site, which produces energy shifts in unoccupied electronic states too large to be accurate.

References

1. Fujishima, A. & Honda, K. Electrochemical Photolysis of Water at a Semiconductor Electrode. *Nature* **238,** 37–38 (1972).
2. Nozik, A. J. Photoelectrochemistry: Applications to Solar Energy Conversion. *Annual Review of Physical Chemistry* **29,** 189–222 (1978).
3. Kato, H. & Kudo, A. Visible-Light-Response and Photocatalytic Activities of TiO_2 and $SrTiO_3$ Photocatalysts Codoped with Antimony and Chromium. *Journal of Physical Chemistry B* **106,** 5029–5034 (2002).
4. Kudo, A. & Miseki, Y. Heterogeneous photocatalyst materials for water splitting. *Chemical Society Reviews* **38,** 253–78 (2009).
5. Zhu, T., Chen, J. S. & Lou, X. W. Highly Efficient Removal of Organic Dyes from Waste Water Using Hierarchical NiO Spheres with High Surface Area. *Journal of Physical Chemistry C* **116,** 6873–6878 (2012).
6. Wang, X. *et al.* A metal-free polymeric photocatalyst for hydrogen production from water under visible light. *Nature Materials* **8,** 76–80 (2009).
7. Maeda, K. *et al.* Overall water splitting on $(Ga_{1-x}Zn_x)(N_{1-x}O_x)$ solid solution photocatalyst: relationship between physical properties and photocatalytic activity. *Journal of Physical Chemistry B* **109,** 20504–20510 (2005).
8. Liu, G., Wang, L., Yang, H. G., Cheng, H.-M. & Lu, G. Q. Titania-based photocatalysts - crystal growth, doping and heterostructuring. *Journal of Materials Chemistry* **20,** 831–843 (2010).
9. Sun, H. *et al.* Origin of the Visible Photocatalytic Activity of N-Doped In_2O_3: A Quantum Mechanical Study. *The Journal of Physical Chemistry C* **114,** 3028–3036 (2010).
10. Tschierlei, S. *et al.* Photochemical fate: the first step determines efficiency of H_2 formation with a supramolecular photocatalyst. *Angewandte Chemie* **49,** 3981–3984 (2010).
11. Kumagai, N., Ni, L. & Irie, H. A visible-light-sensitive water splitting photocatalyst composed of Rh^{3+} in a $4d^6$ electronic configuration, Rh^{3+}-doped $ZnGa_2O_4$. *Chemical communications* **47,** 1884–1886 (2011).
12. Guo, Y., Chu, S., Yan, S., Wang, Y. & Zou, Z. Developing a polymeric semiconductor photocatalyst with visible light response. *Chemical Communications* **46,** 7325–7327 (2010).
13. Schwab, M. G. *et al.* Photocatalytic hydrogen evolution through fully conjugated poly(azomethine) networks. *Chemical Communications* **46,** 8932–8934 (2010).

14. Yi, Z. *et al.* An orthophosphate semiconductor with photooxidation properties under visible-light irradiation. *Nature Materials* **9,** 559–64 (2010).

15. Scott, D. S. *Smelling Land: The Hydrogen Defense Against Climate Catastrophe* ISBN: 1896881734 (Canadian Hydrogen Association, 2008).

16. McDermott, E. J. G. *et al.* Structural and Band Gap Investigation of GaN:ZnO Heterojunction Solid Solution Photocatalyst Probed by Soft X-Ray Spectroscopy. *Journal of Physical Chemistry C* **116,** 7694–7700 (2012).

17. Cabana, J., Monconduit, L., Larcher, D. & Palacín, M. R. Beyond intercalation-based Li-ion batteries: the state of the art and challenges of electrode materials reacting through conversion reactions. *Advanced materials* **22,** E170–192 (2010).

18. Chan, C. K. *et al.* High-performance lithium battery anodes using silicon nanowires. *Nature nanotechnology* **3,** 31–35 (2008).

19. Shankar, R. *Principles of Quantum Mechanics - Second Edition* (Springer, 1994).

20. Schr"odinger, E. Quantisierung als Eigenwertproblem (Vierte Mitteilung. *Annalen der Physik,* 109–139 (1926).

21. Cottenier, S. *Density Functional Theory and the family of (L)APW-methods: a step-by-step introduction* ISBN: 90-807215-1-4 (Instituut voor Kern- en Stralingsfysica, K.U.Leuven, Belgium, 2002).

22. Pohl, R. *et al.* The size of the proton. *Nature* **466,** 213–6 (2010).

23. Born, M. & Oppenheimer, R. Zur Quantentheorie der Molekeln. *Annalen der Physik* **389,** 457–484 (1927).

24. Hohenberg, P. Inhomogeneous Electron Gas. *Physical Review* **136,** B864–B871 (1964).

25. Tran, F. & Blaha, P. Accurate Band Gaps of Semiconductors and Insulators with a Semilocal Exchange-Correlation Potential. *Physical Review Letters* **102,** 226401 (2009).

26. Blaha, P., Schwarz, K., Madsen, G., Kvasnicka, D. & Luitz, J. *WIEN2k, an augmented plane wave + local orbitals program for calculating crystal properties* ISBN: 3-9501031-1-2 (Karlheinz Schwarz, Techn. Universitt Wien, Austria, ISBN: 3-9501031-1-2, 2001).

27. Vretenar, M. Radio frequency for particle accelerators: evolution and anatomy of a technology, 1–14 (2012).

28. Dallin, L. O. *et al.* in *Proceedings of the 2001 Particle Accelerator Conference (Cat. No. 01CH37268)* (IEEE, 2001), 2680–2682. ISBN: 0-7803-7191-7. doi:10.1109/PAC.2001.987871.

29. Lo, C. C., Taylor, B., Lancaster, H. & Guigli, J. in *Proceedings of the 1989 IEEE Particle Accelerator Conference, 1989. Accelerator Science and Technology.* (IEEE, 1989), 956–958.

30. Baptiste, K., Casey, P., Kwiatkowski, S. & Timossi, C. in *2007 IEEE Particle Accelerator Conference (PAC)* (IEEE, 2007), 2307–2309. ISBN: 978-1-4244-0916-7. doi:10.1109/PAC.2007.4441232.

31. Dallin, L. O., Blomqvist, I., de Jong, M., Lowe, D. & Silzer, M. in *Proceedings of the 2003 Bipolar/BiCMOS Circuits and Technology Meeting (IEEE Cat. No. 03CH37440)* (IEEE, 2003), 220–223. ISBN: 0-7803-7738-9. doi:10.1109/PAC.2003.1288884.

32. Tanabe, J., Krupnick, J., Hoyer, E. & Paterson, A. in *Proceedings of International Conference on Particle Accelerators* (IEEE, 1993), 2850–2852. ISBN: 0-7803-1203-1. doi:10.1109/PAC.1993.309482.

33. Hinkson, J. in *Proceedings of the 2001 Accelerator Instrumentation Workshop (LBL-31526)* (1991).

34. Praestegaard, L. *et al.* in *PACS2001. Proceedings of the 2001 Particle Accelerator Conference (Cat. No. 01CH37268)* **5** (IEEE, 2001), 3951–3953. ISBN: 0-7803-7191-7. doi:10.1109/PAC.2001.988308.

35. Attwood, D. *Soft x-rays and extreme ultraviolet radiation: principles and applications* (Cambridge University Press, 2000).

36. Regier, T. *et al.* Performance and capabilities of the Canadian Dragon: The SGM beamline at the Canadian Light Source. *Nuclear Instruments and Methods in Physics Research Section A: Accelerators, Spectrometers, Detectors and Associated Equipment* **582,** 93–95 (2007).

37. Jia, J. J. *et al.* First experimental results from IBM/TENN/TULANE/LLNL/LBL undulator beamline at the advanced light source. *Review of Scientific Instruments* **66,** 1394–1397 (1995).

38. Thompson, A. *X-ray Data Booklet* (Lawrence Berkeley National Laboratory, 2009).

39. Warren, B. *X-Ray Diffraction* (Addison-Wesley, 1969).

40. Attwood, D. *Soft X-rays and Extreme Ultraviolet Radiation* (Cambridge University Press, New York, 1999).

41. The Center for X-Ray Optics, Lawrence Berkeley National Laboratory. *X-Ray Attenuation Length Calculator* http://henke.lbl.gov/optical_constants/atten2.html.

42. McLeod, J. A. *EXAFS Study of Amorphous Selenium* PhD thesis (2010), 124.

43. Hahn, J. E. *et al.* Observation of an electric quadrupole transition in the X-ray absorption spectrum of a Cu(II) complex. *Chemical Physics Letters* **88,** 595 –598 (1982).

44. Von Barth, U. & Grossmann, G. Dynamical effects in x-ray spectra and the final-state rule. *Physical Review B* **25,** 5150–5179 (1982).

45. Lytle, F., Sayers, D. & Stern, E. Extended x-ray-absorption fine-structure technique. II. Experimental practice and selected results. *Physical Review B* **11,** 4825–4835 (1975).

46. Frazer, B. H., Gilbert, B., Sonderegger, B. R. & De Stasio, G. The probing depth of total electron yield in the sub-keV range: TEY-XAS and X-PEEM. *Surface Science* **537,** 161–167 (2003).

47. McLeod, J. A. *et al.* Band gaps and electronic structure of alkaline-earth and post-transition-metal oxides. *Physical Review B* **81,** 245123 (2010).

48. Kurmaev, E. *et al.* Contribution of Fe 3d states to the Fermi level of $CaFe_2As_2$. *Physical Review B* **80,** 1–6 (2009).

49. De Groot, F. High-resolution X-ray emission and X-ray absorption spectroscopy. *Chemical reviews* **101,** 1779–1808 (2001).

50. Morrison, S. R. *Electrochemistry at Semiconductor and Oxidized Metal Electrodes* ISBN: 0-306-40524-5 (Plenum Press, New York, NY, USA, 1980).

51. Bard, A. J. & Faulkner, L. R. *Electrochemical Methods - Fundamentals and Applications - Second Edition* ISBN: 0-471-04372-9 (John Wiley & Sons, New York, 2001).

52. Marcus, R. A. On the Theory of Oxidation-Reduction Reactions Involving Electron Transfer. I. *Journal of Chemical Physics* **24,** 966–978 (1956).

53. Trasatti, S. The Absolute Electrode Potential: An Explanatory Note. *Pure & Appleied Chemistry* **58,** 955–966 (1986).

54. Nozik, A. J. Photoelectrochemistry: Applications to Solar Energy Conversion. en. *Annual Review of Physical Chemistry* **29,** 189–222 (1978).

55. Archer, M. D. & Bolton, J. R. Requirements for ideal performance of photochemical and photovoltaic solar energy converters. *Journal of Physical Chemistry* **94,** 8028–8036 (1990).

56. Licht, S. Multiple Band Gap Semiconductor/Electrolyte Solar Energy Conversion. *Journal of Physical Chemistry B* **105,** 6281–6294 (2001).

57. Doménech, J. & Peral, J. Removal of toxic cyanide from water by heterogeneous photocatalytic oxidation over ZnO. *Solar Energy* **41,** 55–59 (1988).

58. Peral, J., Casado, J. & Doménech, X. Competitive processes in photocatalysis. Phenol-sulphide and phenol-cyanide competitive photooxidation over ZnO. *Electrochimica Acta* **34,** 1335–1338 (1989).

59. Kormann, C., Bahnemann, D. W. & Hoffmann, M. R. Environmental photochemistry: Is iron oxide (hematite) an active photocatalyst? A comparative study: α-Fe_2O_3, ZnO, TiO_2. *Journal of Photochemistry and Photobiology A: Chemistry* **48,** 161–169 (1989).

60. Reber, J. F. & Meier, K. Photochemical production of hydrogen with zinc sulfide suspensions. *Journal of Physical Chemistry* **88,** 5903–5913 (1984).

61. Mayer, M. A. *et al.* Band Gap Engineering of Oxide Photoelectrodes: Characterization of $ZnO_{1-x}Se_x$. *Journal of Physical Chemistry C* **116,** 15281–15289 (2012).

62. Jensen, L., Muckerman, J. & Newton, M. First-Principles Studies of the Structural and Electronic Properties of the $(Ga_{1-x}Zn_x)(N_{1-x}O_x)$ Solid Solution Photocatalyst. *Journal of Physical Chemistry C* **112,** 3439–3446 (2008).

63. Reber, J. F. & Rusek, M. Photochemical hydrogen production with platinized suspensions of cadmium sulfide and cadmium zinc sulfide modified by silver sulfide. *Journal of Physical Chemistry* **90,** 824–834 (1986).

64. Maeda, K. *et al.* GaN:ZnO solid solution as a photocatalyst for visible-light-driven overall water splitting. *Journal of the American Chemical Society* **127,** 8286–8287 (2005).

65. Maeda, K. & Domen, K. Solid Solution of GaN and ZnO as a Stable Photocatalyst for Overall Water Splitting under Visible Light. *Chemistry of Materials* **22,** 612–623 (2010).

66. Maeda, K. & Domen, K. New Non-Oxide Photocatalysts Designed for Overall Water Splitting under Visible Light. *Journal of Physical Chemistry C* **111,** 7851–7861 (2007).

67. Huda, M., Yan, Y., Wei, S.-H. & Al-Jassim, M. Electronic structure of ZnO:GaN compounds: Asymmetric bandgap engineering. *Physical Review B* **78,** 195204 (2008).

68. Wei, W., Dai, Y., Yang, K., Guo, M. & Huang, B. Origin of the Visible Light Absorption of GaN-Rich $Ga_{1-x}Zn_xN_{1-x}O_x$ (x = 0.125) Solid Solution. *Journal of Physical Chemistry C* **112,** 15915–15919 (2008).

69. Di Valentin, C. Electronic Structure of $(Ga_{1-x}Zn_x)N_{1-x}O_x$ Photocatalyst for Water Splitting by Hybrid Hartree-Fock Density Functional Theory Methods. *Journal of Physical Chemistry C* **114,** 7054–7062 (2010).

70. Wang, S. & Wang, L.-W. Atomic and Electronic Structures of GaN/ZnO Alloys. *Physical Review Letters* **104,** 2–5 (2010).

71. Yoshida, M. *et al.* Photoluminescence Spectroscopic and Computational Investigation of the Origin of the Visible Light Response of $(Ga_{1-x}Zn_x)(N_{1-x}O_x)$ Photocatalyst for Overall Water Splitting. *Journal of Physical Chemistry C* **114,** 15510–15515 (2010).

72. Janotti, A. & Van de Walle, C. G. Fundamentals of zinc oxide as a semiconductor. *Reports on Progress in Physics* **72,** 126501 (2009).

73. Stagarescu, C. *et al.* Electronic structure of GaN measured using soft-x-ray emission and absorption. *Physical Review B* **54,** R17335–17338 (1996).

74. Mapa, M. *et al.* Electronic Structure and Catalytic Study of Solid Solution of GaN in ZnO. *Chemistry of Materials* **21,** 2973–2979 (2009).

75. Anisimov, V. I., Aryasetiawan, F. & Lichtenstein, A. I. First-principles calculations of the electronic structure and spectra of strongly correlated systems: the LDA + U method. *Journal of Physics: Condensed Matter* **9,** 767–808 (1997).

76. Cococcioni, M. & de Gironcoli, S. Linear response approach to the calculation of the effective interaction parameters in the LDA+U method. *Physical Review B* **71,** 1–16 (2005).

77. Wyckoff, R. W. G. *Crystal structures - Second Edition* 85–237 (Interscience Publishers, New York, NY, 1963).

78. Perdew, J. P., Burke, K. & Ernzerhof, M. Generalized Gradient Approximation Made Simple. *Physical Review Letters* **77,** 3865–3868 (1996).

79. Hu, C.-C. & Teng, H. Gallium Oxynitride Photocatalysts Synthesized from Ga(OH) 3 for Water Splitting under Visible Light Irradiation. *The Journal of Physical Chemistry C* **114,** 20100–20106 (2010).

80. Li, L., Muckerman, J., Hybertsen, M. & Allen, P. Phase diagram, structure, and electronic properties of $(Ga_{1-x}Zn_x)(N_{1-x}O_x)$ solid solutions from DFT-based simulations. *Physical Review B* **83,** 134202 (2011).

81. Wilks, R. G., MacNaughton, J. B., Kraatz, H.-B., Regier, T. & Moewes, A. Combined X-ray absorption spectroscopy and density functional theory examination of ferrocene-labeled peptides. *Journal of Physical Chemistry B* **110,** 5955–5965 (2006).

82. Han, W., Ward, M. J. & Sham, T. Effect of Indium Doping on the Growth and Physical Properties of Ultrathin Nanosheets of GaInN/ZnO Solid Solution. *Journal of Physical Chemistry C* **115,** 3962–3967 (2011).

83. Han, W.-Q., Liu, Z. & Yu, H.-G. Synthesis and optical properties of GaN/ZnO solid solution nanocrystals. *Applied Physics Letters* **96,** 183112 (2010).

84. Liebig, J. About some nitrogen compounds. *Ann. Pharm* **10,** 10 (1834).

85. Liu, A. Y. & Cohen, M. L. Prediction of new low compressibility solids. *Science* **245,** 841–842 (1989).

86. Niu, C., Lu, Y. Z. & Lieber, C. M. Experimental realization of the covalent solid carbon nitride. *Science* **261,** 334–337 (1993).

87. Wirnhier, E. *et al.* Poly(triazine imide) with Intercalation of Lithium and Chloride Ions $[(C_3N_3)_2(NH_xLi_{1-x})_3 \cdot LiCl]$: A Crystalline 2D Carbon Nitride Network. *Chemistry - A European Journal* **17,** 3213–3221 (2011).

88. Skinner, H. W. B. & Johnston, J. E. Fine-Structure of Soft X-Ray Absorption Edges. I. Li, Mg, Ni, Cu Metals. *Proceedings of the Royal Society A: Mathematical, Physical and Engineering Sciences* **161,** 420–440 (1937).

89. Tsuji, J. *et al.* Lithium K-edge XANES spectra for lithium compounds. *X-Ray Spectrometry* **31,** 319–326 (2002).

90. Braun, A., Wang, H., Shim, J., Lee, S. S. & Cairns, E. J. Lithium K(1s) synchrotron NEXAFS spectra of lithium-ion battery cathode, anode and electrolyte materials. *Journal of Power Sources* **170,** 173–178 (2007).

91. Bergmann, U., Glatzel, P. & Cramer, S. P. Bulk-sensitive XAS characterization of light elements: from X-ray Raman scattering to X-ray Raman spectroscopy. *Microchemical Journal* **71,** 221–230 (2002).

92. Fister, T. T. *et al.* The local electronic structure of α-Li_3N. *Journal of Chemical Physics* **129,** 044702 (2008).

93. Vinson, J., Rehr, J., Kas, J. & Shirley, E. Bethe-Salpeter equation calculations of core excitation spectra. *Physical Review B* **83,** 115106 (2011).

94. Brytov, I. & Kurmaev, E. Z. X-ray Spectral Analysis of the Valence Bands of Oxides of the Iron Group of Transition Metals. *Physics of Metals and Metallography USSR* **32,** 70 (1971).

Appendix A

Calibration References

Table A.1: XES calibration standards

Element	Emission Line	Calibration Material	Energy Peak
Zn	L_3	ZnO	1011.0 eV [94]
Zn	L_2	ZnO	1034.0 eV [94]
O	$K\alpha$	ZnO	526.0 eV [94]
N	$K\alpha$	hexagonal BN	395.2 eV [*]]

Table A.2: XAS calibration standards

Element	Absorption Spectrum	Calibration Material	Energy Peak
O	K 1s	$Bi_4Ge_3O_{12}$	532.7 eV [*]
N	K 1s	hexagonal BN	402.1 eV [*]

[*] $Bi_4Ge_3O_{12}$ and BN features were calibrated against elastically scattered peaks measured on the ALS Beamline 8.0.1 spectrometer.